2021

The Great Plains Irrigation Experiment (GRAINEX)

Eric Rappin
Western Kentucky University, eric.rappin@wku.edu

Rezaul Mahmood
University of Nebraska-Lincoln, rmahmood2@unl.edu

Udaysankar S. Nair
University of Alabama in Huntsville, nair@nsstc.uah.edu

Roger A. Pielke Sr.
University of Colorado at Boulder, pielkesr@cires.colorado.edu

William Brown
National Center for Atmospheric Research, Boulder, CO

See next page for additional authors

Authors

Eric Rappin, Rezaul Mahmood, Udaysankar S. Nair, Roger A. Pielke Sr., William Brown, Steven Oncley, Joshua Wurman, Karen Kosiba, Aaron Kaulfus, Chris Phillips, Emilee Lachenmeier, Joseph A. Santanello Jr., Edward Kim, and Patricia Lawston-Parker

The Great Plains Irrigation Experiment (GRAINEX)

(Submitted to: *Bulletin of the American Meteorological Society*)

Eric Rappin[1], Rezaul Mahmood[2,*], Udaysankar Nair[3], Roger A. Pielke Sr.[4,5], William Brown[6], Steve Oncley[6], Joshua Wurman[7], Karen Kosiba[7], Aaron Kaulfus[3], Chris Phillips[3], Emilee Lachenmeier[2], Joseph Santanello Jr.[8], Edward Kim[8] and Patricia Lawston-Parker[9,8]

[1] Department of Geography and Geology and Kentucky Climate Center, Western Kentucky University, Bowling Green, KY 42101

[2]High Plains Regional Climate Center, School of Natural Resources, University of Nebraska-Lincoln, Lincoln, NE 68583

[3]Department of Atmospheric Science, University of Alabama in Huntsville, Huntsville, AL 35806

[4]Department of Atmospheric and Oceanic Sciences, University of Colorado Boulder, Boulder, CO 80309

[5]Cooperative Institute for Research in Environmental Sciences, University of Colorado Boulder, Boulder, CO 80309

[6]Earth Observation Laboratory, National Center for Atmospheric Research, Boulder, CO 80307

[7]Center for Severe Weather Research, Boulder, CO 80301

[8]NASA Goddard Space Flight Center, MD 20771

[9]Earth System Science Interdisciplinary Center, University of Maryland, College Park, MD 20740

[*] Correspondence to: rmahmood2@unl.edu

Bulletin of the American Meteorological Society
Published-online: 03 May 2021
DOI: https://doi.org/10.1175/BAMS-D-20-0041.1
Page(s): 1–66

Abstract

Extensive expansion in irrigated agriculture has taken place over the last half century. Due to increased irrigation and resultant land use land cover change, the central United States has seen a decrease in temperature and changes in precipitation during the second half of 20^{th} century. To investigate the impacts of widespread commencement of irrigation at the beginning of the growing season and continued irrigation throughout the summer on local and regional weather, the Great Plains Irrigation Experiment (GRAINEX) was conducted in the spring and summer of 2018 in southeastern Nebraska. GRAINEX consisted of two, 15-day intensive observation periods. Observational platforms from multiple agencies and universities were deployed to investigate the role of irrigation in surface moisture content, heat fluxes, diurnal boundary layer evolution, and local precipitation.

This article provides an overview of the data collected and an analysis of the role of irrigation in land-atmosphere interactions on time scales from the seasonal to the diurnal. The analysis shows that a clear irrigation signal was apparent during the peak growing season in mid-July. This paper shows the strong impact of irrigation on surface fluxes, near-surface temperature and humidity, as well as boundary layer growth and decay.

Accepted for publication in *Bulletin of the American Meteorological Society*. DOI 10.1175/BAMS-D-20-0041.1.

Land use land cover changes (LULCCs) play an important role in modulating weather and climate (NRC 2005; Pielke Sr. et al. 2011; Mahmood et al. 2010, 2014; Pielke Sr. et al. 2016). Evidence of its importance can be found in the Third National Climate Assessment (Melillo et al. 2014), Climate Model Intercomparison Project 5 (CMIP5) in support of the 5th Assessment of Climate Change by the IPCC (e.g., Brovkin et al. 2013), LUCID experiments (Pitman et al. 2009), and from the inclusion of LULCC in preparation of CMIP6 (Meehl et al. 2014) in support of the 6th Assessment.

Observations and modeling studies suggest that LULCC impacts meso-, regional-, and potentially global-scale atmospheric circulations, temperature, precipitation, and fluxes (e.g., Segal et al. 1989; Gero et al. 2006; Costa et al. 2007; Campra et al. 2008; Puma and Cook 2010; Davin and de Noblet-Ducoudré 2010; NRC 2012; He et al. 2020; Thiery et al. 2020; Chen et al. 2020). In line with these results, it has been found that agriculture and irrigation significantly impact weather and climate (e.g., Puma and Cook 2010; Sen Roy et al. 2011; Wei et al. 2013; Lawston et al. 2020). In an observational study, Sen Roy et al. (2011) reported up to 69 mm increase in dry season precipitation in the irrigated regions of northwestern India. Based on a modeling study with global focus, Wei et al. (2013) noted ~120 mm increase in annual precipitation in South Asia because of irrigation. Lawston et al. (2020) found 1.67 °C cooling of mean temperatures in the central part of Washington, USA, during summer due to irrigation. Excellent examples of irrigation impacts can be found in the Great Plains (GP) of North America (Barnston and Schickendanz 1984; Mahmood and Hubbard 2002; Adegoke et al. 2003; DeAngelis et al. 2010; Lawston et al. 2015; Szilagyi and Franz, 2020). Barnston and Schickendanz (1984) have shown from observational data that irrigation increases precipitation in the Southern Great Plains. In a follow-up and more detailed study DeAngelis et al. (2010) have also shown that

Accepted for publication in *Bulletin of the American Meteorological Society.* DOI 10.1175/BAMS-D-20-0041.1.

irrigation in the Great Plains impacts precipitation as far as in Indiana and in Kentucky (downwind impact). Mahmood and Hubbard (2002) have conducted a model-based climatological research and found 36% increase in growing season physical evaporation and transpiration (Miralles et al. 2020) due to irrigation and resulted in >1 °C lowering of mean maximum growing season temperature during the second-half of the 20th century over the Northern Great Plains. In a subsequent study, Adegoke et al. (2003) have found similar changes in latent heat fluxes over irrigated areas of Nebraska and further verified previous results.

The irrigated region of the GP extends from Texas to Nebraska and some of the most widespread applications of irrigation can be found in Nebraska (Mahmood and Hubbard 2002). Due to the extent of the GP region, commencement of irrigation each year depends on the start of the growing season which is influenced by local climate and weather in the preceding several months. For example, in the northern part of the GP (northern plains), irrigation typically begins in the latter part of May (e.g., Mahmood and Hubbard 2002).

Commencement of irrigation and its impact on regional hydrometeorology is like a *binary switch* in the Great Plains. Irrigated landscape goes from no irrigation [lower soil moisture (SM)] to fully operational irrigation (higher SM). This switch can occur rapidly over a few days to slightly over a week from a few km^2 to a few thousands km^2 area, respectively. We suggest that impacts on land surface condition, land-atmosphere (L-A) interactions (e.g., Santanello et al. 2018), and the resultant evolution of the boundary layer in and around irrigated areas are significant. Application of irrigation reaches its maximum in July and early August during the plant vegetative growth stage when plant-water requirements are at their highest levels. These intra-seasonal changes impact meso- and regional-scale thermodynamic fields (Mahmood et al. 2004, 2008).

Accepted for publication in *Bulletin of the American Meteorological Society*. DOI 10.1175/BAMS-D-20-0041.1.

Recent work has further supported the need for field campaigns. Gerken et al. (2019) reported that feedbacks between precipitation and land surface fluxes including physical evaporation and transpiration are difficult to observe, but critical for understanding the role of the land surface in the Earth System. As noted previously, in Asia, Sen Roy et al. (2011) reported an increase in dry season rainfall in northwestern India due to irrigation. Devanand et al. (2019) discussed an increase in extreme rainfall in central India in recent decades, and that irrigation increases the rainfall intensity during these events. Their study concluded that it is important to represent irrigation practices more accurately in climate models. Nikiel and Eltahir (2019) reported that a combination of agricultural development and decadal variability of global sea surface temperatures (SST) explains most of the observed variability of summer temperature and precipitation during the twentieth century over central North America.

Despite prior research showing significant potential of irrigated land cover to impact weather, observational campaigns investigating such land-atmosphere interactions are lacking. This paper discusses initial results from such an observational study that investigated the impacts of irrigation on the diurnal evolution of the planetary boundary layer (PBL), cloud development, and precipitation during a field data collection campaign undertaken in southeastern Nebraska. The overall study is known as the Great Plains Irrigation Experiments (GRAINEX) (https://www.eol.ucar.edu/field_projects/grainex). The overarching research goal is to assess:

how irrigation, compared to absence of irrigation, impacts boundary layer development, precipitation and its various characteristics.

Accepted for publication in *Bulletin of the American Meteorological Society.* DOI 10.1175/BAMS-D-20-0041.1.

The results discussed in this paper will improve our understanding of L-A interactions particularly in the context of LULCC and widespread applications of irrigation. Multi-week continuous data collection, analyses of field measurements and modeling provided further insights into L-A interactions. All data analyzed in this study are quality controlled.

Data were collected during the growing season of 2018 in collaboration with the Earth Observation Laboratory's (EOL's) Lower Atmospheric Observation Facilities (LAOF) of the National Center for Atmospheric Research (NCAR), the Center for Severe Weather Research (CSWR), and the Environmental Monitoring, Economical Sensor Hubs (EMESH) system of the University of Alabama in Huntsville. Field data collection efforts included radar wind profilers, radiosonde observations, eddy covariance flux stations, mobile radars known as Doppler on Wheels (DOWs), and a dense surface meteorological network (Fig. 1; details in the following section). In addition, the National Aeronautics and Space Administration (NASA) joined this effort. They have collected data using sensors mounted on a Twin Otter aircraft and further contributed to this study.

Two recent field campaigns, The Soil Moisture–Atmosphere Coupling Experiment (SMACEX) (Kustas et al. 2005) and the International H2O Project (IHOP_2002) (Weckwerth et al. 2004) addressed L-A interactions. In addition, Koster et al. (2004) identified the GP as a 'hotspot' of L-A interactions. However, despite the importance and global expansion of irrigation due to ever-increasing demand for food, these field campaigns and resulting studies did not directly address the role of irrigation in GP weather and L-A interactions. Further, current irrigation schemes in earth system models are rather primitive, and reliant on assumptions about irrigation practices that lack an observational basis (Lawston et al. 2017). We also suggest that GRAINEX is the first experiment of this type, a highly focused project specifically designed to collect data

Accepted for publication in *Bulletin of the American Meteorological Society.* DOI 10.1175/BAMS-D-20-0041.1.

over contrasting and adjacent irrigated and non-irrigated regions to study irrigation impacts. Due to the uncertain role of irrigation impacts on precipitation, the results presented here make a fundamental contribution to that aspect of L-A interactions.

Field Experiment Overview and Data Collection

The GRAINEX field campaign took place in southeastern Nebraska over a ~100 x 100 km area comprised of adjacent irrigated and non-irrigated land from the end of May until the beginning of August (Fig. 1). Nebraska was selected as it is one of the most highly irrigated regions of the world, and the most irrigated state of the USA. The Big Blue River in southeastern Nebraska separates extensively irrigated croplands to the west and non-irrigated cropland to the east (Fig. 1).

Two intensive-observation periods (IOPs) were selected with a much more extensive observational array (as discussed below) for: 1) 05/29/18 – 06/13/18 (IOP1), and 2) 07/16/18 – 07/30/18 (IOP2). IOP1dates were chosen to capture the commencement of irrigation, or *binary switch*, during which there is a rapid change in moisture availability occur. IOP2 dates were selected to investigate land-atmosphere interactions at the height of the growing season when crop-water demand and irrigation applications area also at a maximum.

Observational platforms include Integrated Surface Flux System (ISFS), Integrated Sounding System (ISS), Radiosondes, DOW, and Environmental Monitoring, Economical Sensor Hubs (EMESH) (Fig. 2a-h). Details of the observations can be found in https://www.eol.ucar.edu/field_projects/grainex. These details include, among others, description of instrumentation and data quality. Below we provide a brief description of these observation platforms and their deployment design.

Accepted for publication in *Bulletin of the American Meteorological Society*. DOI 10.1175/BAMS-D-20-0041.1.

Integrated Surface Flux System (ISFS)

To determine irrigation impacts, six ISFS were deployed over irrigated and six ISFS over non-irrigated areas (Figs. 1, 2a-d, and Table 1). All of the irrigated ISFS sites are located over the western part of the study area, while non-irrigated sites are over the eastern part. As can be found from Table 1, all sites measured standard above surface meteorological variables, including, temperature, pressure, relative humidity, rainfall, wind speed and direction, and solar radiation. These sites also measured fluxes of momentum as well as sensible and latent heat at a rate of 50 samples per second. To complete measurements, each site recorded soil moisture, soil temperature, soil heat capacity, and soil heat flux (Table 2). While all sites were operational continuously from about mid-May to mid-August, the ISS and DOWs were only available during the IOPs. As a result, focus is given to these periods. ISFS data were communicated in near real-time via cell modem to EOL/LAOF. These data subsequently went through quality control checks and were delivered as five-minute average observations.

Integrated Sounding System (ISS)

Two ISS sites were instrumented to help understand the response of PBL to land surface conditions (irrigated vs. non-irrigated) (Figs. 1 and 2e). One of these sites was located over an open area at York airport away from runaway and clutter. This small county airport is located just outside of York, NE and surrounded by extensively irrigated crop fields. A second site was located in Rogers Memorial Farm (Short: Rogers Farm), east of Lincoln, NE (Table 3a) representing the non-irrigated region of eastern NE. Both sites included radar wind profiler, ceilometer, and standard surface meteorological observations (Table 3b). Additionally, both sites simultaneously launched radiosondes every two hours from sunrise [~ 5:00 AM Local Standard Time (~1100

Accepted for publication in *Bulletin of the American Meteorological Society.* DOI 10.1175/BAMS-D-20-0041.1.

UTC); there is a six hour lag in Local standard Time compared to UTC (LST = UTC - 0600)] to sunset [~7:00 PM Local Standard Time (~0100 UTC)] resulting in 8 launches per site per day (Fig. 2f). The data were collected for both IOP1 and IOP2. In short, a comprehensive set of data were collected to understand properties and evolution of the boundary layer during the IOPs over irrigated and non-irrigated regions of the study domain. These observations were also complementary to ISFS observations.

Doppler on Wheels (DOW)

Three X-band DOWs (Wurman 2001) were deployed in a configuration that allowed for data to be collected over irrigated, non-irrigated, and over irrigated to non-irrigated transition zones (Fig. 1 and 2g) to further capture fine-scale evolution of the PBL (Wurman et al. 2021; Wurman and Kosiba 2020). DOW reflectivity and Doppler velocity fields were used to identify atmospheric boundaries in the PBL. These observations were used in conjunction with the other observations in this paper. In addition, the radar data will be used in the future to further investigate the impact of irrigation on PBL development and convective processes. From the three DOW locations, radiosondes (Graw DFM-09) were launched simultaneously in coordination with the ISS sites. Thus, there were about 40 launches per day from the five locations (~1200 total) to sample the atmosphere and the evolution of the PBL.

Environmental Monitoring, Economical Sensor Hubs (EMESH)

To further complement these observations and to better capture small-scale surface and near-surface variations, a network of 75 meteorological stations known as EMESH were deployed from late May 2018 through mid-August 2018 covering both IOPs (Figs. 1, 2h and Table 4).

Accepted for publication in *Bulletin of the American Meteorological Society.* DOI 10.1175/BAMS-D-20-0041.1.

EMESH are rapidly deployable weather stations that were developed at the University of Alabama in Huntsville. For this research project, 28 stations were deployed over irrigated and 47 over non-irrigated areas. Of these 75 stations, 50 and 25 were deployed during the IOP1 and IOP2, respectively. They were successfully field tested for their accuracy and reliability prior to the deployment for this project. Each of these stations recorded standard meteorological parameters as well as soil moisture and temperature (Table 4). This paper does not include analysis of EMESH data.

NASA Goddard Radio Frequency Explorer (GREX) Instrument

The GREX microwave (L-band) radiometer was mounted on the NASA Twin Otter plane and was utilized during the IOP2, conducting seven flights from 07/16/18 through 07/27/18 measuring radiances at a spatial resolution < 1 km. The GREX mission was to measure spatial patterns and transects of soil moisture across and between the ground stations. GREX, coupled with a suitable antenna, measures brightness temperature similar to that of the Soil Moisture Active-Passive (SMAP) satellite. For GRAINEX, the L-Band front-end operated within a 1400-1427 MHz frequency range as is utilized by the SMAP radiometer. GREX was setup to match SMAP's single channel soil moisture algorithm inputs for the GRAINEX deployment. The motivation for flying GREX was to observe spatial surface heterogeneity over the GRAINEX domain and to connect with point-based soil moisture measurements and their variability across the region. Results from GREX data are not included in this paper.

Accepted for publication in *Bulletin of the American Meteorological Society*. DOI 10.1175/BAMS-D-20-0041.1.

Results

Overall Weather Conditions During IOP1 and IOP2

During IOP1 eastern Nebraska was on the southern edge of the polar jet which was comparatively far south for the time of year (Archer and Caldeira 2008; Pielke Sr. 2018). The position of the jet resulted in several occurrences of rain from mesoscale convective systems forced by upper-level troughs. The overall result of this pattern were several rain events and occasional cooler and drier days after the cold fronts passed. The synoptic weather pattern during IOP2 was similar to IOP1. Thus, there were extended sunny and partly sunny periods punctuated by showers and thunderstorms.

Surface Meteorological Conditions

Key quantities including 2-m temperature, mixing ratio, and soil moisture at the ISFS sites, averaged over irrigated (blue) and non-irrigated (red) cropland sites are shown in Fig. 3a-c. All of these observations are recorded at 5-minute intervals and then averaged. IOP1 and IOP2 were during the first and last two weeks, respectively and displayed in the panels. The differences in temperature, mixing ratio, and soil moisture between irrigated and non-irrigated land uses are shown on the right axis of Fig. 3a-c. In order to minimize the noise of the seasonal figures, the difference calculations are only done at a single time each day, the time of maximum temperature, as averaged over irrigated or non-irrigated cropland. While this does eliminate any response lag between the two croplands, it captures an overall seasonal characteristics.

The 2-m temperature and mixing ratio (Fig. 3a-b) reveal that there were two distinct observed near-surface weather conditions. During IOP1 and prior to 1 July, on average, there was only a relatively smaller observed difference in temperature and mixing ratio between irrigated

Accepted for publication in *Bulletin of the American Meteorological Society*. DOI 10.1175/BAMS-D-20-0041.1.

and non-irrigated croplands. In contrast, during IOP2 and the month of July, as expected, there was a much larger observed difference between irrigated and non-irrigated croplands. During this period, on average, the mean daily temperature over irrigated areas was reduced by -0.69ºC because of increased physical evaporation from soils and transpiration from crops. This is reflected in an increased mixing ratio of +1.54 g kg^{-1}.

GRAINEX was also designed to investigate the *binary switch* of the onset and subsequent sustained irrigation on near-surface meteorology and L-A interactions. Due to frequent weather events during IOP1 and much of June, the *binary switch* did not occur until the beginning of July. The large-scale forcing (Supplementary Fig. 1a-c) can be observed in the near-surface meteorology shown in Fig. 3a-c, which displays frequent large-amplitude fluctuations in the temperature (Fig. 3a) and mixing ratio (Fig. 3b) suggestive of frontal passages on weekly timescales.

Closer inspection of Fig. 3a reveals a small downward trend in the difference in mean maximum temperature (statistically significant at 99% confidence level) between the irrigated and non-irrigated sites from mid-June through late July. The downward trend would be expected under an irrigation signal during the growing season. It is because latent heat fluxes dominate energy partition over irrigated areas (please see 'Surface Fluxes' section below for further details). The 2-m mixing ratio shows a relatively clear response to irrigation with larger values over irrigated cropland (Fig. 3b). In addition, volumetric soil moisture content displayed in Fig. 3c shows the impact of precipitation and irrigation, or lack thereof. While it is difficult to isolate the relative roles, there were clear irrigation signals on 8 July (blue spike in the absence of a red spike) and 24 July – 27 July and light precipitation over irrigated cropland on 23 July.

Accepted for publication in *Bulletin of the American Meteorological Society.* DOI 10.1175/BAMS-D-20-0041.1.

Due to the observed delay in irrigation onset, IOP1 will be discussed in a rather limited fashion. Attention will be given to IOP2, in particular for the L-A interactions from 22 July to 24 July.

Surface Fluxes

Data from ISFS sites over irrigated and non-irrigated sites were analyzed for IOP1 and IOP2. Analyses and comparisons are completed for 5, 15, and 30 minute flux data and it is found that the results are quite similar (Supplementary Figure 2a-d). Thus, since this paper presents initial results and overview of the GRAINEX, 5 minute data are used. It is evident from Fig. 4a-f that, overall, the latent heat fluxes were higher compared to the sensible heat fluxes during both IOP1 and IOP2. During the early growing season (IOP1) differences between latent and sensible heat fluxes were not as large as IOP2. However, during peak-growing season (IOP2) water consumption is higher by plants and the resultant application of irrigation caused increased partitioning of the available energy into the latent heat fluxes. For example, Fig. 4a shows that during the early growing season (IOP1), latent heat fluxes were mainly lower (Fig. 4a-b) over irrigated sites. Frequent changes in weather accompanied by cloud cover suppressed overall heat fluxes. On the other hand, during peak-growing season (IOP2), latent heat fluxes were mostly greater over the same locations. As noted in the previous section and above, synoptic weather-wise IOP1 was more active which depressed fluxes in both irrigated and non-irrigated locations. In addition, Fig. 4e-f also shows that on average for all sites, latent (sensible) heat fluxes were consistently higher (lower) during the second IOP2.

There were noticeable decreases in temperature and increases in mixing ratio over irrigated areas, particularly during the last 10 days of IOP2 (Fig. 5a-f). In addition, during the entire month

Accepted for publication in *Bulletin of the American Meteorological Society*. DOI 10.1175/BAMS-D-20-0041.1.

of July, near-surface temperatures were found to be approximately 1°C cooler while near-surface humidity are 2 g kg^{-1} moister for irrigated land use (compare with black curves in Fig. 3). Since the moisture contribution was significantly large, equivalent potential temperature (θ_E) increased over irrigated cropland. This result is borne out in Fig. 5c where the near-surface θ_E shows an increase over irrigated land use relative to non-irrigated. Note that, compared to irrigated areas, there were small time lags in reaching of mixing ratio, and θ_E over non-irrigated areas. In the morning boundary layer evolution was quite similar at all locations with the rapid growth of surface fluxes and boundary layer height through mid-morning (~1000 LST). After this time, temperatures rose at a lower rate over irrigated land use as opposed to non-irrigated due to higher soil moisture over irrigated areas. Moreover, we suggest that as latent heat fluxes increased rapidly over irrigated areas, highest values were reached slightly earlier over irrigated land use compared to non-irrigated land use. This particularly reflected in mixing ratio and θ_E values.

Examination of the 2.5 cm soil moisture evolution (Fig. 5d) for the last ten days of IOP2 shows the diurnal variability and increases due to precipitation and irrigation. Note that the irrigated sites have larger soil moisture values reflective of irrigation prior to and during IOP2. Irrigation applications occur in response to crop-water requirements and soil moisture status and linked to its distribution between field capacity (higher limit) and wilting point (lower limit). As expected, farmers typically do not wait until soil moisture reaching the wilting point and hence soil moisture for irrigated croplands typically varies between field capacity and wilting point. During GRAINEX, the noted differences in near-surface temperature, mixing ratio, and 2.5 cm soil moisture are associated with the observed surface sensible and latent heat fluxes (Fig. 5e-f). In the absence of cloud cover, the sensible heat fluxes increase while the latent heat fluxes decrease by at the non-irrigated ISFS sites. In short, compared to non-irrigated locations, higher latent heat

Accepted for publication in *Bulletin of the American Meteorological Society*. DOI 10.1175/BAMS-D-20-0041.1.

fluxes from the irrigated locations lowered temperature and increased θ_E and mixing ratio. On the other hand, sensible heat fluxes dominated over non-irrigated area resulting in higher temperature and lower mixing ratio.

During the first half of the 20-29 July period (IOP2), the near-surface daily maximum temperature remained unchanged near 28 ºC over irrigated sites while non-irrigated sites were on average about 1ºC warmer (Fig. 5a). Due to predominantly clear conditions and higher soil moisture over irrigated areas, physical evaporation and transpiration depleted the soil moisture more rapidly over irrigated sites than over non-irrigated sites (Fig. 5d). The near-surface mixing ratio also decreased (Fig. 5b) due to dry air advection from the north. Sensible heating increased over the first five days as a result of fair weather except for 23 July which brought overcast conditions and light precipitation to the boundary between irrigated and non-irrigated croplands. Latent heat fluxes decreased across the study area as soil moisture was depleted. However, there was a rebound late on 23 and 24 July after the light rains. The second half of the IOP2 displayed periods of heavier precipitation over irrigated sites on 25 July (primarily at site 6 but also at sites 1 through 4) and on 27 July (site 1) and non-irrigated sites on 28 July (most sites). Overcast conditions lowered surface fluxes on 25 July except for the physical evaporation that occurred after heavy rainfall over irrigated sites. The lack of precipitation led to large sensible heat fluxes over non-irrigated sites until precipitation arrived on 28 July. At this point the sensible heating and temperature were lowered while the latent heating increased.

In contrast to the northerly flow that dominated late July, during the inter-IOP period of early July, deep tropospheric ridging occurred and L-A interactions are expected to dominate. Fig. 6a-d displays the near-surface temperature, mixing ratio and surface energy fluxes during the week of 5 to 12 July. Warm southerly flow dominated the boundary layer during this time leading to

Accepted for publication in *Bulletin of the American Meteorological Society.* DOI 10.1175/BAMS-D-20-0041.1.

increases in temperature and evaporative demand resulting in the applications of irrigation. An example of irrigation can be found in site 6 where on 8 July the volumetric soil moisture nearly doubled from 20% to 40% (not shown). Since there was no precipitation but positive changes in soil moisture, we suggest applications of irrigation. These applications of irrigation resulted in 2 °C cooler temperatures over irrigated sites compared to non-irrigated sites. In this context, we suggest that the average latent heat flux over irrigated cropland was higher relative to that over non-irrigated cropland due to the irrigation applied on 8 July. With southerly flow and increasing temperature, evaporative demand also increased resulting in higher latent heat fluxes and near-surface mixing ratios. Due to synoptic-scale high pressure settings and weak winds, on a number of nights there were dual maximum in mixing ratio which is not uncommon. One such peak in mixing ratio occurred just prior to the peak in latent heating. Note that after the sunrise the atmospheric boundary layer becomes unstable with further solar radiation leading to development of convection and mixing down of dry air above the inversion in the atmosphere and subsequent lowering of the mixing ratio. In the late afternoon, as sun angle lowers and longwave radiation becomes dominant over incoming shortwave radiation, the convective boundary layer decouples from the surface, and the nighttime inversion layer begins to form. The latter traps any residual physical evaporation and transpiration and leads to late afternoon-evening maximum.

Diurnal observations of 22-24 July 2018

Synoptic Evolution

To further understand irrigated and non-irrigated differences, we focus on a 3-day period of 22-24 July 2018 during which two L-A interactions case days occurred and were separated by a day of weak large-scale ascent and light precipitation. To investigate the L-A interactions in

Accepted for publication in *Bulletin of the American Meteorological Society*. DOI 10.1175/BAMS-D-20-0041.1.

adjacent irrigated and non-irrigated cropland during the three-day period, three data sets are utilized: 1) ISFS observations of near-surface temperature, dew point temperature, soil moisture, accumulated precipitation, and surface fluxes at each site; 2) ISS wind profiler data of wind speed, wind direction, and signal-to-noise ratio at both the York (irrigated) and Rogers Farm (non-irrigated) sites, and 3) ISS radiosonde data of potential temperature, virtual potential temperature, and skew-T diagrams at both sites.

The synoptic setting with plots of the surface and 300 hPa analyses from the NOAA Storm Prediction Center are shown in Fig. 7a-f for 1800 LST, 22 July (0000 UTC, 23 July) and 0600 LST, 23 July (1200 UTC, 23 July) and 1800 LST, 23 July (0000 UTC, 24 July). At 300 hPa, the GRAINEX domain was between a large stationary high-pressure system centered in the southwest US and a negatively tilted trough in the eastern US that extended from Minnesota to the Florida panhandle. By the end of the period on 24 July, the flow was largely zonal as the northern flank of the southeastern high expanded with the eastward propagation of the Canadian low.

During the morning and early afternoon of 23 July, a cold front moved through the GRAINEX study area with satellite and camera imagery showing persistent overcast conditions (not shown) and fog. While a T-shaped thunderstorm complex developed north of the GRAINEX area, the meridional portion of the complex extends southward east of the area while a new north-south oriented rain band developed over the irrigated area starting at 0600 LST (Figure 8a-i). The rain line grew in strength as it slowly propagated across the irrigated cropland and dissipated as it moved over the non-irrigated area (discussed further in the next section). Finally, on 24 July, surface high pressure with clear skies and low wind speeds settled over the GRAINEX area providing ideal conditions for strong L-A interactions.

Accepted for publication in *Bulletin of the American Meteorological Society.* DOI 10.1175/BAMS-D-20-0041.1.

PBL Evolution of 22-24 July, 2018 as Observed by ISFS, ISS, and DOWs

On 22 July, near-surface atmospheric conditions (Fig. 9a-e) over the study area are saturated between 0300 and 0600 LST (Fig. 9a-b). With light winds, radiation fog is evident over the York site from camera images (not shown) that dissipates at sunrise and has completely disappeared due to boundary layer mixing by 0700 LST. The fog/cloud cover over irrigation is also evident from the temperature and dew point temperature in Fig. 9a-b where they remain steady between 0300 and 0600 LST but continue to fall over the non-irrigated locations. As observed in Fig. 5b, the mean mixing ratio over non-irrigated cropland falls to a lower value than over irrigated. The lower value was likely due to dew formation, as the temperature continued to fall, along with the dew point, at a faster rate over non-irrigated cropland (Fig 9a-b). The fog (dew) over irrigated (non-irrigated) cropland is further reflected in the negative sensible heat fluxes between 0300 and 0600 LST (Fig. 9e) as the surface warmed by increasing net radiation. Sites 6 and 7 were located along the irrigation-non-irrigation boundary (Figure 1) and took on characteristics of both types of land uses. For example, site 7 (pink), a non-irrigated site, displayed the diurnal temperature characteristics of the irrigated sites.

There was no precipitation on 22 July and the largest soil moisture values were found at the irrigated locations (Fig. 9c). The sensible and latent heat fluxes for each site on 22 July are shown in Fig. 9d and e. Once the sky was cloud-free, between 0600 and 0700 LST, the air and dew point temperature quickly rose in association with the increases in sensible and latent heat fluxes, respectively. In addition, the fluxes began to reflect the land surface wetness between 1000 to 1500 LST when sensible heat flux decreased and latent heat flux increased. It is during these times when the air and dew point temperature also started to diverge between the two different types of land uses (Fig. 9a-b).

Accepted for publication in *Bulletin of the American Meteorological Society*. DOI 10.1175/BAMS-D-20-0041.1.

Figure 10a-d displays the wind speed and wind direction at both ISS sites on 22 July. Light winds dominated the boundary layer outside of a near-surface wind maxima around 250 m that formed around late evening and did not subside until sunrise. Above the boundary layer, stronger winds persisted over Rogers Farm as a cold front approached York from the west. Rogers Farm area was under the influence of stronger pressure gradient compared to York and northwest flow that existed above the boundary layer. Conversely, the flow aloft became westerly and diffluent over York. After sunrise the PBL height (PBLH) increased, as observed in the wind profilers signal-to-noise ratio at each site (Fig. 10e-f), until reaching a maximum height in the early afternoon (i.e., just after noon local time). Note the white and black curve in the figures showing the PBLH as determined by the Bulk Richardson number (Vogelezang and Holtslag 1996; Seidel et al. 2012) and the lifting condensation level (LCL; Bolton 1980), respectively. Given the larger sensible heat fluxes over non-irrigated cropland, the maximum boundary layer height attained a higher altitude, just over 1 km AGL, compared to PBLH over irrigation, which grew to around 850 m.

The soundings for 22 July reveal a stronger stable surface layer at the Rogers Farm ISS site compared to that of the York site (Supplementary Fig. 3a-d). In terms of PBLH, the peak height occurred at the 1300 LST sounding in York while the maximum in Rogers Farm occurred at the 1500 LST sounding, again indicative of the larger sensible heating over the non-irrigated region. However, the weak surface inversion at York permitted its more rapid growth compared to the strong surface stratification prior to sunrise at Rogers Farm. It is also evident from the soundings that there was a capping inversion over York. Therefore, the lower PBLH at York can be contributed to both weaker sensible heat fluxes and a stronger capping inversion. Finally, the pre-sunrise skew-T log*p* plots (Fig. 10g-h) show the moister boundary layer over irrigation with a

Accepted for publication in *Bulletin of the American Meteorological Society*. DOI 10.1175/BAMS-D-20-0041.1.

much shallower dry layer limited to the region of sharp direction wind shear in the entrainment layer. Over Rogers Farm, the entrainment layer was much thicker extending from 1 to 2 km AGL. Note that the entrainment was maximum after the morning transition, bringing drier air from above the inversion into the PBL and surface layer which increased evaporative demand and a response from the irrigated and non-irrigated vegetation.

Much different conditions presented themselves on 23 July as the surface front moved into the GRAINEX study area (Fig. 7a-b). Similarity of air and dew point temperature at irrigated sites suggests that air was saturated at 2 m roughly from 0000 LST to 0800 LST, 23 July while the non-irrigated sites were close to saturation from 0400 LST to 0800 LST, 23 July (Supplementary Fig. 4a-b). The overcast conditions also led to decreased surface fluxes on 23 July (Supplementary Fig. 4c-d). However, rain fell over irrigated sites (discussed below) in the morning hours so the sensible heat fluxes were constrained. The front passed through the entire GRAINEX region by around 1400 LST 23 July, leaving behind mostly sunny skies prior to the afternoon-evening transition. As a result, a stable boundary layer developed across the entire region as evidenced by the negative sensible heat fluxes across all sites.

An increase (decrease) in dew point was observed over irrigated (non-irrigated) sites between 0600 LST and 1400 LST (1200 to 1600 LST, although there was a slight increase as the sun rose and latent heating commenced), a result of PBL entrainment from above and the continued physical evaporation and transpiration. Advection is assumed to be small, given boundary layer winds that are generally calm and rarely exceed 5 m s^{-1}. Weak large-scale advection may also suggest why the air and dew point temperature at 2 m largely followed the diurnal surface flux evolution. The winds increased from the north after 1500 LST on 23 July over irrigated (not

Accepted for publication in *Bulletin of the American Meteorological Society.* DOI 10.1175/BAMS-D-20-0041.1.

shown) and after 1800 LST on 23 July over non-irrigated (not shown) areas which caused the dew points to decline rapidly over both land uses (Supplementary Fig. 4a-b).

As discussed in the synoptic evolution, a convective line associated with a cold front extended from western Minnesota to just west of the GRAINEX area with a southwest-northeast orientation at around 0300 LST on 23 July. While the precipitation was broken up west of the GRAINEX area, it maintained intensity on the north side of the domain. Subsequently, as the cold front propagated east-southeast across the northern portion of the GRAINEX region, a line developed east of Rogers Farm, NE. Around 0600 LST a meridional convective line developed directly over DOW8 (Fig. 8a-c), moved eastward and intensified as it approached DOW6 and DOW7 (Fig. 8d-f), and stalled and decayed over and eastward of DOW6 and DOW7 around 0730 LST (Fig. 8g-i). Given the development of this system during IOP2, a more detailed integrated observational and modeling analysis will be provided in a future publication.

The Most Unstable Convective Available Potential Energy (MUCAPE) is shown in Fig. 11a-c and is calculated using a reversible moist adiabat with ice. The use of MUCAPE to characterize buoyancy mitigates inaccuracies that early morning inversions can have on surface-based CAPE calculations. By the late morning, however, standard surface-based CAPE and MUCAPE are typically equivalent. On 22 July (Fig. 11a), MUCAPE is relatively small and constant throughout the sounding period of the day. It is worth noting that MUCAPE over the irrigated York ISS site is consistently larger (blue curve) than that of the non-irrigated Rogers Farm ISS site (red curve). On 23 July (Fig 11b), MUCAPE was suppressed during the precipitation event at 1300 UTC but quickly rebounded due to the near saturated conditions that exist throughout the day in the lower troposphere. The MUCAPE increased rapidly in the western, irrigated sites (DOW8, ISS-York) followed by the other two DOW sites that straddle the irrigation

Accepted for publication in *Bulletin of the American Meteorological Society.* DOI 10.1175/BAMS-D-20-0041.1.

gradient (DOW6 and DOW7) and at the non-irrigated ISS-Rogers Farm site. Unsurprisingly, MUCAPE declined to low values on 24 July (Fig. 11c).

One of the best examples of local L-A interactions during IOP2 was on 24 July (Fig. 12a-f). High pressure had settled in over the GRAINEX study area (Fig. 7e-f) with clearing during overnight hours leading to rapid temperature decline (Fig. 12a). In addition, a faster temperature decline occurred over irrigated sites as the dew point temperature (Fig. 12b) had already begun to lower after the frontal passage late on 23 July from 1800 to 2400 LST (first half of the local evening). During the second half of the local evening/early morning, 0000 LST to 0600 LST, 23 July the irrigated sites cooled to the dew point and dew formed. Several non-irrigated cropland does not quite reach saturation during the overnight cooling period. During the first six hours after sunrise, from 0600 to 1200 LST, there was a rapid increase in 2-m temperature (Fig. 12a), and a decrease in both PBL and lower tropospheric wind speeds mostly in the north-northeasterly direction (Fig. 13a-d) with PBL growth at both sites was observed (Fig. 13e-f). The dew point temperature also increases with daybreak likely due to the physical evaporation of dew. In addition, diverging of the 2-m temperature, humidity, and surface fluxes (Fig. 12) between irrigated and non-irrigated locations on 24 July provides a clear example of the role of irrigation on near-surface meteorology.

At the end of 24 July, the winds became southeasterly. The PBL grew rapidly and was well mixed over both ISS sites by 1100 LST as can be found in both the signal-to-noise ratio (Fig. 13e-f) and radiosondes (Fig. 14a-f). The LCL at both sites (black curves in Fig. 13e-f) increased rapidly after sunrise, well before the PBL mixed layer developed, to 3 km over irrigated and above 4 km on non-irrigated croplands after which little variation was observed until the after-evening transition. The morning sounding over irrigated York shows a classic nocturnal boundary layer

Accepted for publication in *Bulletin of the American Meteorological Society*. DOI 10.1175/BAMS-D-20-0041.1.

structure with a strong inversion (nearly 10ºC in the lowest 250 m) underlying a weakly stable layer that extends up to 1.25 km. In contrast, over non-irrigated Rogers Farm the layer overlying the strong inversion was neutral. Further inspection of data suggests that vertical shear existed between 500 and 1000 m at both locations from 0100 LST to 0700 LST (Figure 13 a-b). The shear was stronger over non-irrigated Rogers Farm so that shear production and breaking waves may force this layer toward neutral stratification compared to the weakly stable conditions over York. The absence of vertical turbulence profiles prohibited further investigation and verifying this hypothesis. There was a slightly stronger capping inversion over irrigation as observed in the potential temperature and virtual temperature soundings (Fig. 14a-d) while PBL top entrainment was stronger over the non-irrigated ISS site in Rogers Farm as indicated by the higher PBLH. In the afternoon, observed PBLH has stabilized over irrigation at just above 1 km. On the other hand, the PBLH decreased over Rogers Farm by late afternoon to a value similar to that over York by 1700 LST. Although it is more pronounced over the Rogers Farm, the PBLH decreased over both location by sunset.

Mixing Diagrams

The ISS-York (in close proximity to ISFS site 2) and the ISS-Rogers Farm (in close proximity to ISFS site 9) (Fig. 1) is used to approximate land surface states, near-surface meteorology, and atmospheric profile data in order to produce mixing diagrams (Fig. 15a-f). Mixing diagrams were introduced by Betts (1982, 1992). They were further highlighted by Santanello et al. (2009, 2011, 2018) as a tool for diagnosing local land-atmosphere interactions. Mixing diagrams are a vector approach to describing the diurnal growth and decay of the convective boundary layer from a heat and moisture budget perspective. The methodology

Accepted for publication in *Bulletin of the American Meteorological Society.* DOI 10.1175/BAMS-D-20-0041.1.

employs a boundary layer moist static energy (MSE) column budget approach for the understanding of L-A interactions by considering fluxes through the bottom boundary (surface fluxes), lateral boundaries (advection), and top boundary (entrainment). For the analysis carried out here, only surface fluxes were utilized with entrainment calculated as a residual as described in the documentation for L-A interactions metrics produced for GEWEX/GLASS (http://cola.gmu.edu/dirmeyer/Coupling_metrics.html). Small magnitude processes, such as advection and non-adiabatic terms are contained as part of the entrainment term.

Four quantities that are difficult to observe but can be obtained from mixing diagrams (Santanello et al. 2009, 2011) are: 1) the surface Bowen ratio ($\beta_s = SH_s / LH_s$), 2) the entrainment Bowen ratio ($\beta_e = SH_e / LH_e$), 3) the latent heat entrainment ratio ($A_l = LH_e / LH_s$), and 4) the sensible heat entrainment ratio ($A_h = SH_e / SH_s$). In these 4 quantities, subscripts l, h, e, and s represent latent heating, sensible heating, evaluation in the entrainment layer, and evaluation at the surface, respectively. Note that in Fig. 15 a, c, and e, the dashed lines are vectors representing the surface and entrainment fluxes and yield the Bowen Ratio of the surface and entrainment (Santanello et al. 2019). The values of the quantities for each of the days considered is shown in Table 5, where the daily mean values are given. Two hourly values were also calculated, corresponding to the sounding time interval, which resulted in similar values to that of the daily mean when aggregated, as was observed in Santanello et al. (2009).

On 22 July, the morning hours were dominated by warming and moistening at both locations (Fig. 15a), resulting in decreasing relative humidity but increasing equivalent potential temperature (Fig. 15b). Close to noon (1100 LST), the PBLH had attained its largest value capping a well-mixed boundary layer. The larger PBLH over Rogers Farm suggests a greater entrainment of warm, dry air from the free troposphere resulting in warming, and slight drying of the 2-m air

Accepted for publication in *Bulletin of the American Meteorological Society.* DOI 10.1175/BAMS-D-20-0041.1.

as can be observed in the mixing diagram (Fig. 15a), leading to a near constant θ_e and declining relative humidity (Fig. 15b). There was minimal drying at 2 m over York and while the humidity went down (rapidly in the morning, then slowly in the afternoon), θ_e increased throughout the day. In other words, at mid-day solar heating dominated the surface Bowen Ratio evolution with entrainment drying dominating the Rogers Farm signature while surface moistening from physical evaporation at York resulted in the maintenance of a positive slope to the surface Bowen Ratio. Prior to sunset (the darkest dots in Figs 15a-b) there was a period of moistening leading to a rise in relative humidity at both sites. This period of moistening and slow cooling is associated with increased moisture flux convergence during the afternoon-evening transition. One point worth considering is that southeastern Nebraska experiences a humid continental climate, not semi-arid where L-A interactions is significantly more pronounced. Furthermore, spring and summer of 2018 were wet and there were clear differences between soil moisture over irrigated and non-irrigated croplands as reflected in the ISFS soil moisture plots (Figs. 8c and 12c).

The daily mean surface (entrainment) Bowen ratio has a value nearly 3 (1.5) times larger over non-irrigated cropland compared to irrigated cropland. It is suggestive of the larger magnitude of sensible heating and smaller magnitude of latent heat fluxes over non-irrigated areas (Fig. 15a-b). The surface Bowen ratio was maximized in the morning and decreased throughout the day (not shown) as both latent and sensible heat fluxes were increased with relative magnitudes being larger at both locations. This is, again, indicative of the most rapid boundary layer growth occurring between sunrise and noon local time. At noon local time, the surface Bowen ratio difference between irrigated and non-irrigated cropland was maximized where it was three times larger over non-irrigated areas compared to the irrigated. The entrainment layer Bowen ratio was similar to that of the surface, although it was typically negative given that warm (positive heat flux) and dry

Accepted for publication in *Bulletin of the American Meteorological Society*. DOI 10.1175/BAMS-D-20-0041.1.

air (negative moisture flux) entrained into the boundary layer from the free atmosphere. Again, the most negative values were found in the morning with increasing values throughout the day, turning positive just before and during the evening transition (not shown). The entrainment ratios are much more similar in magnitude (Table 5) in terms of the daily aggregate, with the moisture entrainment flux being significantly larger over irrigated land uses due to the overall weaker entrainment coupled with a larger surface moisture flux. The same can be said for the non-irrigated areas, where the heat fluxes at both the surface and the entrainment layer are maximized in late morning and decreased proportionally through the afternoon.

On 23 July, the frontal passage, as discussed in the synoptic evolution, led to a much different mixing diagram than the previous day (Fig. 15c-d). Due to cloud cover inhibiting long wave radiative cooling, surface air temperatures remained high overnight. Also, the moisture term in moist static energy at sunrise was the same as at sunset of the previous night at Rogers Farm but has decreased slightly at York. The 2-m temperature increased at both sites during the morning hours, but the 2-m humidity remains near constant at Rogers Farm, resulting in a decreasing relative humidity and a near constant θ_e (Fig. 15c-d). At ISS-York, the near-surface moisture increased rapidly in the morning as the squall line developed between the York site and the Big Blue River. The mixing ratio began to fall rapidly well before the temperature started to decrease, providing further support of a frontal passage prior to sunset. In contrast, the ISS-Lincoln site underwent moistening until a few hours before sunset at which point the temperature began to fall, moistening weakened, and drying commenced with frontal passage at the final observation time (1900 LST 24 July 2018). As a result, both relative humidity and θ_e decreased with time in the afternoon at York. On the other hand, relative humidity decreased and θ_e increased with time at Rogers Farm until just prior to sunset. In terms of daily aggregates, the surface Bowen ratio at

Accepted for publication in *Bulletin of the American Meteorological Society.* DOI 10.1175/BAMS-D-20-0041.1.

Rogers Farm was 5 times larger than that at York while the entrainment layer Bowen ratio magnitude at York was 3 times that at Rogers Farm. The surface Bowen ratio can be explained with the aid of Supplementary Fig. 4c-d where the latent heat flux was about 25% larger over irrigated cropland compared to non-irrigated. The smaller magnitude of latent heat flux over Rogers Farm was therefore responsible for the consistently larger surface Bowen ratio. Unlike 22 July, the entrainment ratios were quite different at the two sites. The entrainment layer Bowen ratio and entrainment heat and moisture fluxes must be carefully considered as the overcast moist day did not provide ideal conditions for L-A observations as observed in the soundings (not shown). As noted above, advective tendencies in the moist static energy budget are difficult to assess in an observational study and will be addressed in a forthcoming modeling study.

On 24 July, conditions were similar to 22 July with high surface pressure and cloud free skies. The strong cooling and drying after the frontal passage led to the lowest values observed in moist static energy at sunrise. The latent and sensible heat components of moist static energy increased in a similar manner during the morning hours (Fig. 15e-f) until the mixed layer had grown to near the PBLH and entrainment is effective at modifying the surface temperature and humidity. With the temperature and moisture increasing, θ_e increased slightly as the relative humidity plummeted. During the afternoon, dry air originating out of the north entrained into the PBL from the free atmosphere. As discussed previously, the ISS-Rogers Farm site observed drier air capping the inversion as the winds at York became westerly on 24 July in advance of another precipitation system that arrived on 25 July (not shown). As a result, and in contrast to the two previous days, the entrainment layer Bowen ratio has a larger magnitude over York than over Rogers Farm and the moisture term of moist static energy over York was lower than that of Rogers Farm.

Accepted for publication in *Bulletin of the American Meteorological Society.* DOI 10.1175/BAMS-D-20-0041.1.

Conclusions

The Great Plains Irrigation Experiment (GRAINEX) was conducted in the spring and summer of 2018 to investigate the role of the sudden onset and continued widespread application of irrigation on PBL evolution and near-surface meteorology in southeastern Nebraska which includes adjacent irrigated and non-irrigated areas. GRAINEX is the first of this type of field campaign that has solely focused on the impacts of irrigated versus non-irrigated land uses on the atmosphere. This study is particularly important and timely in the context of rapid expansion of irrigated agriculture globally and its potential impacts on weather and climate. This paper presented initial results of analysis of data from GRAINEX.

The study finds that early in the growing season (IOP1), differences in temperatures between irrigated and non-irrigated regions were relatively small compared to the middle of the growing season (IOP2) with cooler temperatures over irrigated areas during both time periods. The observed mixing ratio also showed similar patterns with higher mixing ratios over irrigated land. Generally, the daily differences between latent and sensible heat fluxes were also smaller during the early growing season over both irrigated and non-irrigated land while they were larger during the peak growing season over irrigated areas. Consistent with these findings, higher soil moisture and lower turbulent kinetic energy was reported during the peak growing season and planetary boundary height was lower over irrigated land (Fig. 16).

Observations also demonstrate the influence of irrigation on the daily evolution of these variables as well as MUCAPE, Bowen ratio, equivalent potential temperature, planetary boundary layer height and several other land-atmosphere interaction measures. In addition, initial assessment suggests that irrigated land use may have influenced precipitation events over the study area. Future studies will include additional assessment of the observed data from the GRAINEX and

Accepted for publication in *Bulletin of the American Meteorological Society*. DOI 10.1175/BAMS-D-20-0041.1.

numerical modeling to further understand the process and mechanisms via which irrigated and non-irrigated land use impacts lower troposphere and weather.

Acknowledgements: The authors would like to thank three anonymous reviewers for their valuable comments and suggestions which helped to improve this paper. This research is funded by the NSF grants AGS-1853390 (Rezaul Mahmood and Eric Rappin), AGS-1720477 (Udaysankar Nair), and AGS-1552487 (Roger Pielke Sr.). Thanks to team members from the NCAR/Lower Atmosphere Observation Facilities and the Center for Severe Weather Research for operating ISS, ISFS, and DOW observation platforms. The NASA Science Utilization of SMAP program (PM: Jared Entin) supported GREX deployment and the participation of Joseph Santanello, Edward Kim, and Patricia Lawston-Parker. Thanks go to additional NASA personnel Albert Wu, Rajat Bindlish, Pilots and support staff for the Twin Otter where GREX was mounted, and NASA affiliated students. Feedbacks provided during project development by Kevin Knupp and Paul Dirmeyer are gratefully acknowledged. The PIs of the project are also grateful to Nebraska Extension personnel, including, Randy Pryor, Aaron Nygren, Gary Lesoing, Tyler Williams, Brandy VandeWalle, and Jenny Reese; Nebraska's Natural Resources Districts personnel Dick Ehrman, Chuck Wingert, Tyler Benal, Rod DeBuhr, Daryl Anderson; and to Al Dutcher and Stonie Cooper of Nebraska State Climate Office. Together they played a key role in site selection and connecting PIs to nearly one hundred landowners. Access to land for siting observation platforms was critical to success of the GRAINEX project and the PIs are thankful for the generosity of the landowners. Thanks also to Adam Houston for recruiting students from the Department of Earth and Atmospheric Science, University of Nebraska-Lincoln (UNL), who assisted in the field work. Similarly, thanks go to students of the School of Natural Resources,

Accepted for publication in *Bulletin of the American Meteorological Society.* DOI 10.1175/BAMS-D-20-0041.1.

UNL and the Meteorology Program, Department of Geography and Geology, Western Kentucky University. Thanks to Dallas Staley for her excellent technical editing.

Accepted for publication in *Bulletin of the American Meteorological Society*. DOI 10.1175/BAMS-D-20-0041.1.

References:

Adegoke, J.O., R. A. Pielke, J. Eastman, R. Mahmood, and K. G. Hubbard, 2003: Impact of irrigation of midsummer surface fluxes and temperature under dry synoptic conditions: A regional atmospheric model study of the U.S. High Plains. *Mon. Wea. Rev.*, **131,** 556-564.

Archer, C. L. and K. Caldeira, 2008: Historical trends in the jet streams. *Geophys. Res. Lett.* **35,** L08803, doi:10.1029/2008GL033614.

Barnston, A., and P. T. Schickedanz, 1984: The effect of irrigation on warm season precipitation in the Southern Great Plains. *J. Climate Appl. Meteorol.,* **23,** 865–888.

Bolton, D., 1980: The computation of equivalent potential temperature. *Mon. Wea. Rev.* **108,** 1046-1053.

Brovkin, V, L. Boysen, V. K. Arora, J. P. Boisier, P. Cadule, L. Chini, M. Claussen, P. Friedlingstein, V. Gayler, B. J. J. M. Van Den Hurk, G. C. Hurtt, C. D. Jones, E. Kato, N. de Noblet- Ducoudré, F. Pacifico, J. Pongratz, and M. Weiss, 2013: Effect of anthropogenic land-use and land-cover changes on climate and land carbon storage in CMIP5 Projections for the Twenty-First Century. *J. Climate*, **26,** 6859-6881.

Campra P., M. Garcia, Y. Canton, and A. Palacios-Orueta, 2008: Surface temperature cooling trends and negative radiative forcing due to land use change toward greenhouse farming in southeastern Spain. *J. Geophys. Res.*, **113,** D18109. DOI: 10.1029/2008JD009912.

Chen, C. J., C. C. Chen, M. H. Lo, J. Y. Juang, and C. M. Chang, 2020: Central Taiwan's hydroclimate in response to land use/cover change. *Env. Res. Lett.,* **15,** 034015.

Costa, M. H., S. N. M. Yanagi, P. J. O. P. Souza, A. Ribeiro, and E. J. P. Rocha, 2007: Climate change in Amazonia caused by soybean cropland expansion, as compared to caused by pastureland expansion. *Geophys. Res. Lett.*, **34,** L07706. DOI: 10.1029/2007GL029271.

Davin, E.L., and N. de Noblet- Ducoudré, 2010: Climatic impact of global-scale deforestation: radiative versus nonradiative processes. *J. Climate*, **23,** 97–112.

DeAngelis, A., F. Dominguez, Y. Fan, A. Robock, M. D. Kustu, and D. Robinson, 2010: Evidence of enhanced precipitation due to irrigation over the Great Plains of the United States. *J. Geophys. Res.,* **115,** D15115, doi:10.1029/2010JD013892.

Devanand, A., M. Huang, M. Ashfaq, B. Barik, and S. Ghosh, 2019: Choice of irrigation water management practice affects Indian summer monsoon rainfall and its extremes. *Geophys. Res. Lett.,* **46,** 9126-9135.

Accepted for publication in *Bulletin of the American Meteorological Society.* DOI 10.1175/BAMS-D-20-0041.1.

Gerken, T., B. L. Ruddell, R. Yu, P. C. Stoy, and D. T. Drewry, 2019: Robust observations of land-to-atmosphere feedbacks using the information flows of FLUXNET. *Climate Atmos. Sci.*, **2,** 1-10.

Gero, A.F., A. J. Pitman, G. T. Narisma, C. Jacobson, and R. A. Pielke, 2006: The impact of land cover change on storms in the Sydney Basin, Australia. *Glob. Planet. Change*, **54,** 57-78.

He, Y., E. Lee, and J. S. Mankin, 2020: Seasonal tropospheric cooling in Northeast China associated with cropland expansion. *Env. Res. Lett*. **15,** 034032.

Koster, R. D., P. A. Dirmeyer, Z. Guo, G. Bonan, E. Chan, P. Cox, C. T. Gordon, S. Kanae, E. Kowalczyk, D. Lawrence, P. Liu, Cheng-Hsuan Lu, S. Malyshev, B. McAvaney, K. Mitchell, D. Mocko, T. Oki, K. Oleson, A. Pitman, Y. C. Sud, C. M. Taylor, D. Verseghy, R. Vasic, Y. Xue, and T. Yamada, 2004: Regions of strong coupling between soil moisture and precipitation. *Science*, **305,** 1138-1140.

Kustas, W. P., J. L. Hatfield, and J. H. Prueger, 2005: The soil moisture–atmosphere coupling experiment (SMACEX): Background, hydrometeorological conditions, and preliminary findings. *J. Hydrometeor.*, **6,** 791-804.

Lawston, P. M., J. A. Santanello Jr., B. F. Zaitchik, and M. Rodell, 2015: Impact of irrigation methods on land surface model spinup and initialization of WRF Forecasts. *J. Hydrometeor.*, **16,** 1135– 1154.

Lawston, P. M., J. A. Santanello Jr., T. E. Franz, and M. Rodell, 2017: Assessment of irrigation physics in a land surface modeling framework using non-traditional and human-practice datasets. *Hydrol. Earth Syst. Sci.*, **21,** 2953–2966.

Lawston, P. M., J. A. Santanello Jr., B. Hanson, and K. Arsensault, 2020: Impacts of irrigation on summertime temperatures in the Pacific Northwest. *Earth Inter.*, **24,** 1-26.

Mahmood, R., and K. G. Hubbard, 2002: Anthropogenic land-use change in the North American tall grass-short grass transition and modification of near-surface hydrologic cycle. *Climate Res.*, **21,** 83-90.

Mahmood, R., K. G. Hubbard, and C. Carlson, 2004: Modification of growing season surface temperature records in the Northern Great Plains due to land use transformation: verification of modeling results and implication for global climate change. *Int. J. Climatol.*, **24,** 311-327.

Mahmood, R., K. G. Hubbard, R. Leeper, and S. A. Foster, 2008: Increase in near surface atmospheric moisture content due to land use changes: Evidence from the observed dew point temperature data. *Mon. Wea. Rev.*, **136,** 1554-1561.

Accepted for publication in *Bulletin of the American Meteorological Society.* DOI 10.1175/BAMS-D-20-0041.1.

Mahmood, R., R. A. Pielke Sr., K. G. Hubbard, D. Niyogi, G. Bonan, P. Lawrence, B. Baker, R. McNider, C. McAlpine, A. Etter, S. Gameda, B. Qian, A. Carleton, A. Beltran-Przekurat, T. Chase, A. I. Quintanar, J. O. Adegoke, S. Vezhapparambu, G. Conner, S. Asefi, E. Sertel, D. R. Legates, Y. Wu, R. Hale, O. N. Frauenfeld, A. Watts, M. Shepherd, C. Mitra, V. G. Anantharaj, S. Fall, R. Lund, A. Nordfelt, P. Blanken, J. Du, H-I., Chang, R. Leeper, U. S. Nair, S. Dobler, R. Deo, and J. Syktus, 2010: Impacts of land use land cover change on climate and future research priorities. *Bull. Amer. Meteor. Soc.*, **91,** 37-46.

Mahmood, R., R. A. Pielke Sr., K. G. Hubbard, D. Niyogi, P. Dirmeyer, P., C. McAlpine, A. Carleton, R. Hale, S. Gameda, A. Beltran-Przekurat, B. Baker, R. McNider, D. R. Legates, M. Shepherd, J. Du, P. Blanken, O. W. Frauenfeld, U. S. Nair, and S. Fall, 2014: Land cover changes and their biogeophysical effects on climate. *Int. J. Climatol.*, **34,** 929–953.

Meehl, G. A., R. Moss, K. E. Taylor, V. Eyring, R. J. Stouffer, S. Bony, and B. Stevens, 2014: Climate model intercomparison: Preparing for the next phase. *Eos, Trans. AGU*, 95(9), 77.

Melillo, J. M., T. Richmond, and G. W. Yohe, 2014: *Climate Change Impacts in the United States: The Third National Climate Assessment.* U.S. Global Change Research Program, 841 pp.

Miralles, D. G., W. Brutsaert, A. J. Dolman, and J. H. Gash, 2020: On the use of the term "evapotranspiration". *Water Resources Research*, *56*, e2020WR028055. https://doi.org/10.1029/2020WR028055

NRC (National Research Council), 2005: *Radiative Forcing of Climate Change: Expanding the Concept and Addressing Uncertainties.* The National Academies Press: Washington, D.C.

NRC (National Research Council), 2012: *Urban Meteorology: Scoping the Problem, Defining the Need*. The National Academies Press: Washington, D.C.

Nikiel, C. A., and E. A. Eltahir, 2019: Summer climate change in the Midwest and Great Plains due to agricultural development during the twentieth century. *J. Climate*, **32,** 5583-5599.

Pielke Sr., R. A. 2018. Daily Weather Discussions. Version 1.0. UCAR/NCAR – Earth Observing Laboratory. https://data.eol.ucar.edu/dataset/561.010. Accessed August 2019.

Pielke Sr., R.A., A. Pitman, D. Niyogi, R. Mahmood, C. McAlpine, F. Hossain, K. Klein Goldewijk, U. Nair, R. Betts, S. Fall, M. Reichstein, P. Kabat, and N. de Noblet-Ducoudré, 2011: Land use/land cover changes and climate: Modeling analysis and observational evidence. *Wiley Interdisc. Rev.: Climate Change* **2,** 828-850.

Accepted for publication in *Bulletin of the American Meteorological Society*. DOI 10.1175/BAMS-D-20-0041.1.

Pielke Sr., R. A., R. Mahmood, and C, McAlpine, 2016: Land's complex role in climate change. *Phys. Today*, **69,** 40-46.

Pitman, A.J., N. De Noblet- Ducoudré , F. T. Cruz, E. Davin, G. Bonan, V. Brovkin, M. Claussen, C. Delire, L. Ganzeveld, V. Gayler, B. Van Den Hurk, P. Lawrence P, M. Van Der Molen, C. Muller, C. Reick, S. Seneviratne, B. Strengen, and A. Voldoire, 2009: Uncertainties in climate responses to past land cover change: First results from the LUCID intercomparison study', *Geophys. Res. Lett.* **36,** L14814, http://dx.doi.org/10.1029/2009GL039076

Puma, M. J., and B. I. Cook, 2010: Effects of irrigation on global climate during the 20th century. *J. Geophys. Res.,* **115,** D16120. DOI: 10.1029/2010JD014122.

Santanello, J. A, C. D. Peters-Lidard, S. V. Kumar, C. Alonge, and W.-K. Tao, 2009: A modeling and observational framework for diagnosing local land–atmosphere coupling on diurnal time scales. *J. Hydrometeor.*, **10,** 577–599.

Santanello, J. A., C. D. Peters-Lidard, and S. V. Kumar, 2011: Diagnosing the sensitivity of local land–atmosphere coupling via the soil moisture–boundary layer interaction. *J. Hydrometeor.*, **12,** 766–786.

Santanello, J. A., P. A. Dirmeyer, C. R. Ferguson, K. L. Findell, A. B. Tawfik, A. Berg, M. Ek, P. Gentine, B. P. Guillod, C. van Heerwaarden, J. Roundy, and V. Wulfmeyer, 2018: Land–atmosphere interactions: The LoCo perspective. *Bull. Amer. Meteor. Soc.*, **99,** 1253–1272.

Segal, M., J. R. Garratt, R. A. Pielke, W. E. Schreiber, A. Rodi, G. Kallos, and J. Weaver, 1989: The impact of crop areas in northeast Colorado on midsummer mesoscale thermal circulations. *Mon. Wea. Rev.*, 117: 809-825.

Seidel, D. J., Zhang, Y., Beljaars, A., Golaz, J. C., Jacobson, A. R. and B. Medeiros, 2012: Climatology of the planetary boundary layer over the continental United States and Europe. *Journal of Geophysical Research: Atmospheres*, 117(D17).

Sen Roy, S. , R. Mahmood, A. I. Quintanar, and A. Gonzalez, 2011: Impacts of irrigation on dry Season precipitation in India. *Theor. Appl. Climatol.*, 104: 193-207, DOI: 10.1007/s00704-010-0338-z.

Szilagyi, J., and T. E. Franz, 2020: Anthropogenic hydrometeorological changes at a regional scale: observed irrigation–precipitation feedback (1979–2015) in Nebraska, USA. *Sustain. Water Resour. Manag.*, **6,** 1. https://doi.org/10.1007/s40899-020-00368-w

Thiery, W., A. J. Visser, E. M. Fischer, M. Hauser, A. L. Hirsch, D. M. Lawrence, Q. Lejeune, E. L. Davin, and S. I. Seneviratne, 2020: Warming of hot extremes alleviated by expanding irrigation. *Nature Comm.*,

Accepted for publication in *Bulletin of the American Meteorological Society.* DOI 10.1175/BAMS-D-20-0041.1.

https://doi.org/10.1038/s41467-019-14075-4

Weckwerth, T. M., D. B. Parsons, S. E. Koch, J. A. Moore, M. A. LeMone, B. B. Demoz, C. Flamant, B. Geerts, J. Wang, and W. F. Feltz, 2004: An overview of the international H2O project (IHOP_2002) and some preliminary highlights. *Bull. Amer. Meteor. Soc.*, **85,** 253-257.

Wei, J., P. A. Dirmeyer, D. Wisser, M. C. Bosilovich, and D. M. Mocko, 2013: Where does the irrigation water go? An estimate of the contribution of irrigation to precipitation using MERRA. *J. Hydrometeor.*, **14,** 275-289.

Wurman, J., 2001: The DOW mobile multiple Doppler network. *Preprints, 30th Int. Conf. on Radar Meteorology*, Munich, Germany, Amer. Meteor. Soc., 95–97.

Wurman, J., and K. Kosiba, 2020:. FARM-data-GRAINEX (Version 1) [Data set]. Center for Severe Weather Research. https://doi.org/10.48514/6XTH-M998

Wurman, J., K. Kosiba, B. Pereira, P. Robinson, A. Frambach, A. Gilliland, T. White, J. Aikins, R. J. Trapp, S. Nesbitt, M. N. Hanshaw, J. Lutz, 2021: The FARM (Flexible Array of Radars and Mesonets. *Bull. Amer. Meteor. Soc.,* (in review).

Xu, X., Y. Jiang, M. Liu, Q. Huang, and G. Huang, 2019: Modeling and assessing agro-hydrological processes and irrigation water saving in the middle Heihe River basin. *Agricultural Water Management*, **211,** 152-164.

Accepted for publication in *Bulletin of the American Meteorological Society.* DOI 10.1175/BAMS-D-20-0041.1.

Table 1. GRAINEX ISFS sites and their locations.

Site	Nearest Town	Latitude (deg N)	Longitude (deg W)	Land use land cover	Flux Sensor Mounting Height (m)
1	Benedict	41.009669	-97.541247	Irrigated	6
2	York	40.879614	-97.541887	Irrigated	6
3	Exeter	40.66228	-97.4846	Irrigated	6
4	Beaver Crossing	40.77854	-97.33173	Irrigated	6
5	Friend	40.662223	-97.333542	Irrigated	6
6	Wilber	40.458504	-97.028949	Irrigated	6
7	Loma	41.135725	-96.974423	Non-irrigated	4.5
8	Panama	40.57374	-96.461773	Non-irrigated	6.5
9	Elmwood	40.8238	-96.33517	Non-irrigated	6.5
10	Unadilla	40.645905	-96.271274	Non-irrigated	6.5
11	Unadilla	40.6932	-96.223161	Non-irrigated	4.5
12	Cook	40.483095	-96.202562	Non-irrigated	5.5

Accepted for publication in *Bulletin of the American Meteorological Society*. DOI 10.1175/BAMS-D-20-0041.1.

Table 2. Parameters measured at each GRAINEX ISFS sites.

Parameter	Sensor	Mounting Height/depth (m)
Air temperature, relative humidity	NCAR TRH	2
Air pressure	Vaisala PTB220, PTB2010 barometers; Paroscientific nanobarometer	2
Fluxes of momentum, sensible and latent heat, and carbon dioxide	Campbell CSAT3A/EC150	4.5-6
Horizontal wind speed/direction	Gill WindObserver 2D sonic anemometer	10
Precipitation (rain)	MRI tipping bucket	2
Radiation (4-components)	Hukseflux NR01 integrated radiometer	2
Soil heat capacity	Hukseflux TP01	0.025
Soil heat flux	REBS HFT	0.05
Soil moisture	Decagon EC-5	0.025
Soil temperature profile	NCAR Tsoil	0-0.05

Accepted for publication in *Bulletin of the American Meteorological Society*. DOI 10.1175/BAMS-D-20-0041.1.

Table 3a. Location of ISS sites.

Site	Description	Latitude (deg N)	Longitude (deg W)
ISS2	Rogers Memorial Farm	40.8444	-96.4683
ISS3	York Municipal Airport	40.8916	-97.6261

Table 3b. Measurements at the ISS locations (Rogers Memorial Farm & York Municipal Airport).

System	Measurement	Sensor
Upper Air	Cloud Height	Vaisala CL31 and CL51 Ceilometer
	Sounding Variables	Vaisala MW41/RS 41 Radiosondes
	Wind Profile	LAP3000 915 MHz DBS radar wind profiler with RASS
Surface	Pressure	Vaisala PTB210
	Radiation (4-components)	Hukseflux NR01
	Precipitation (rain)	HAS Tipping Bucket
	Meteorological Summary - Temperature - Relative humidity - Precipitation type - Precipitation intensity - Precipitation quantity - Air pressure - Wind direction - Wind speed - Radiation	Lufft WS700/800 Weather Sensors

Accepted for publication in *Bulletin of the American Meteorological Society*. DOI 10.1175/BAMS-D-20-0041.1.

Table 4. Measured parameters at each EMESH station during the GRAINEX.

Parameter	Sensor	Mounting Height/depth (m)
Air Temperature	BOSCH BMP 180, Sensirion SHT 75	2
Barometric Pressure	BOSCH BMP 180	2
Relative Humidity	Sensirion SHT 75	2
Wind speed	Davis Vantage Pro 2	3
Wind direction	Davis Vantage Pro 2	3
Rainfall	Sparkfun Tipping Rain gauge	2
Soil temperature	Maxim DS18B20	-0.05, -0.3
Volumetric soil moisture	METER Group EC-5	-0.05, -0.3

Accepted for publication in *Bulletin of the American Meteorological Society*. DOI 10.1175/BAMS-D-20-0041.1.

Table 5. Mixing Diagram Bowen and Entrainment Ratios (York/Lincoln)

	β_s (York/Lincoln)	β_e (York/Lincoln)	A_l (York/Lincoln)	A_h (York/Lincoln)
22 July 222018	0.11/0.27	-0.35/-0.57	-0.68/-0.65	2.2/1.4
23 July 2018	0.05/0.24	-0.22/-0.75	-0.48/-0.92	3.93/1.54
24 July 2018	0.09/0.29	-0.70/-0.55	-0.61/-0.84	4.75/1.58

Accepted for publication in *Bulletin of the American Meteorological Society*. DOI 10.1175/BAMS-D-20-0041.1.

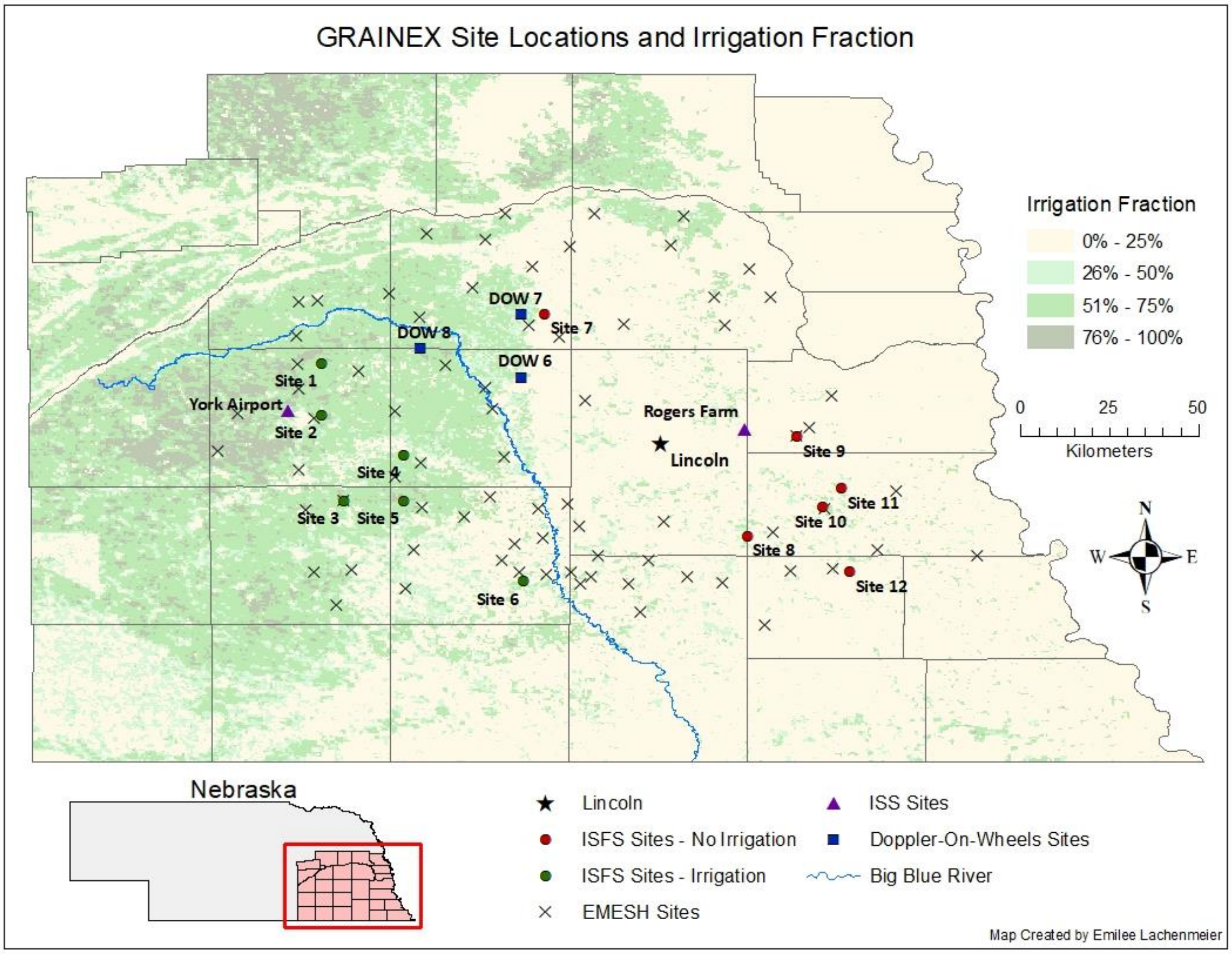

Fig. 1. Location of various observation platforms over eastern Nebraska. The region transitions from non-irrigated (in the east) to irrigated (in the west) areas.

Accepted for publication in *Bulletin of the American Meteorological Society.* DOI 10.1175/BAMS-D-20-0041.1.

a)

Accepted for publication in *Bulletin of the American Meteorological Society.* DOI 10.1175/BAMS-D-20-0041.1.

b)

Accepted for publication in *Bulletin of the American Meteorological Society*. DOI 10.1175/BAMS-D-20-0041.1.

c)

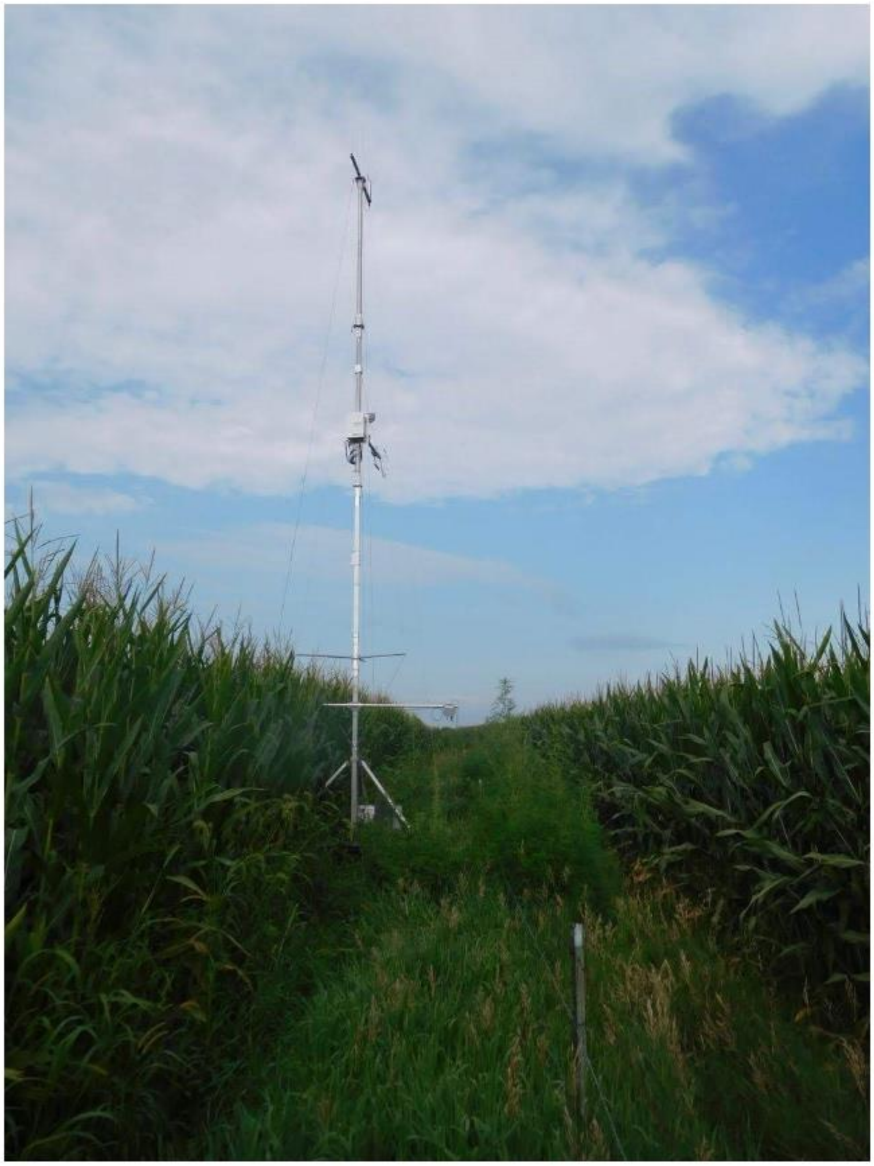

Accepted for publication in *Bulletin of the American Meteorological Society*. DOI 10.1175/BAMS-D-20-0041.1.

d)

Accepted for publication in *Bulletin of the American Meteorological Society*. DOI 10.1175/BAMS-D-20-0041.1.

e)

Accepted for publication in *Bulletin of the American Meteorological Society.* DOI 10.1175/BAMS-D-20-0041.1.

f)

Accepted for publication in *Bulletin of the American Meteorological Society*. DOI 10.1175/BAMS-D-20-0041.1.

g)

Accepted for publication in *Bulletin of the American Meteorological Society.* DOI 10.1175/BAMS-D-20-0041.1.

h)

Fig. 2a-h. a) An irrigated ISFS tower (site #1 in Fig. 1) at the beginning of the IPO2 with a center pivot irrigation system in the background; b) a tripod with net radiometer during IOP1, c) same ISFS tower during IOP2 (middle of the growing season; d) net radiometer during IOP2 (middle of the growing season); e) ISS radar wind profiler; f) a launched radiosonde balloon; g) one of the three Doppler on Wheels (DOW) and h) an EMESH station next to an irrigated field.

Accepted for publication in *Bulletin of the American Meteorological Society*. DOI 10.1175/BAMS-D-20-0041.1.

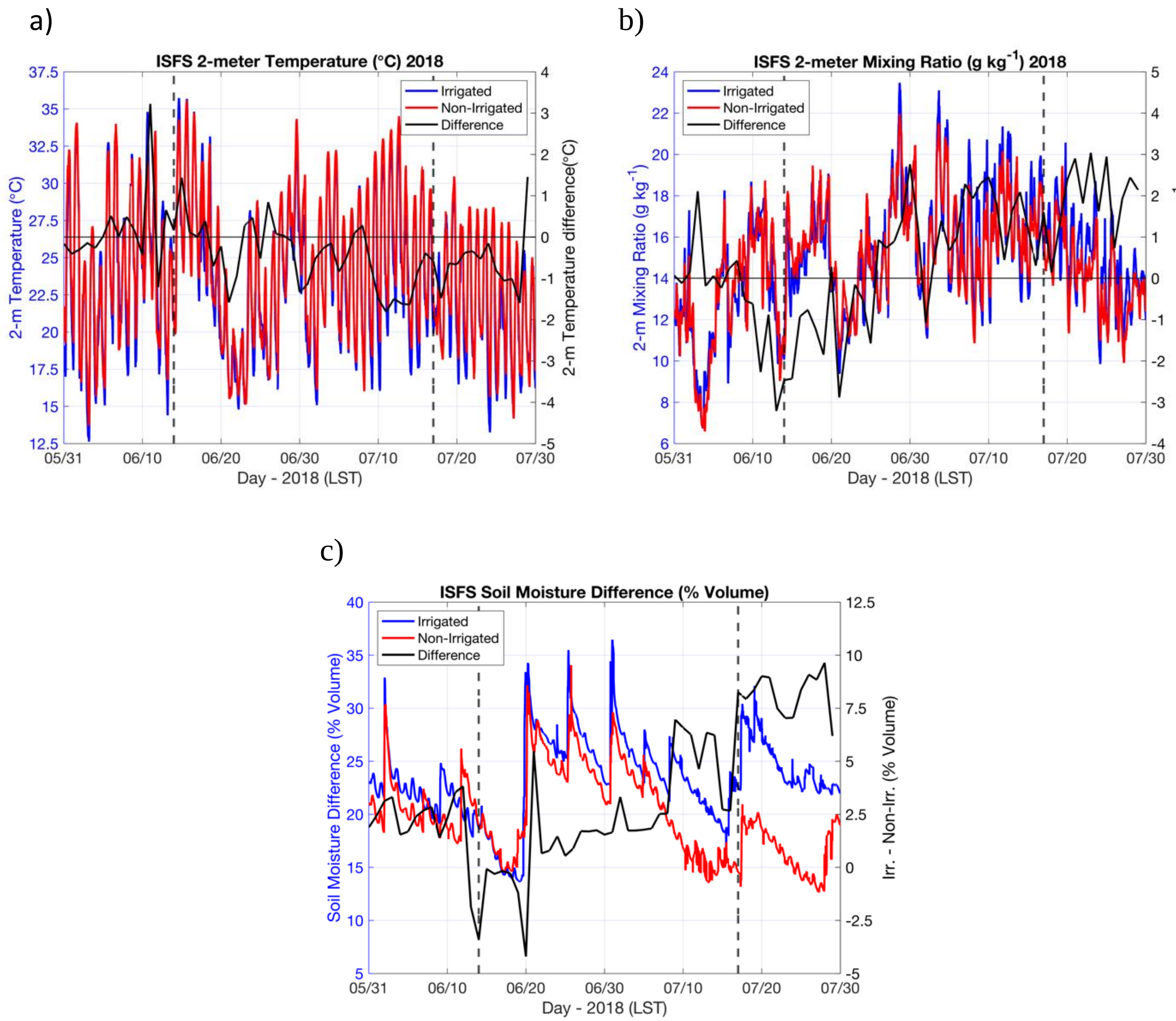

Fig. 3a-d. Average 2-m a) temperature; b) mixing ratio; and c) soil moisture for irrigated and non-irrigated ISFS sites with their differences at the time of their respective daily maximum temperature. These panels included IOP1, IOP2, and the period in-between IOP1 and IOP2 (time between two dashed vertical lines). Horizontal line represents zero difference between irrigated and non-irrigated sites.

a)

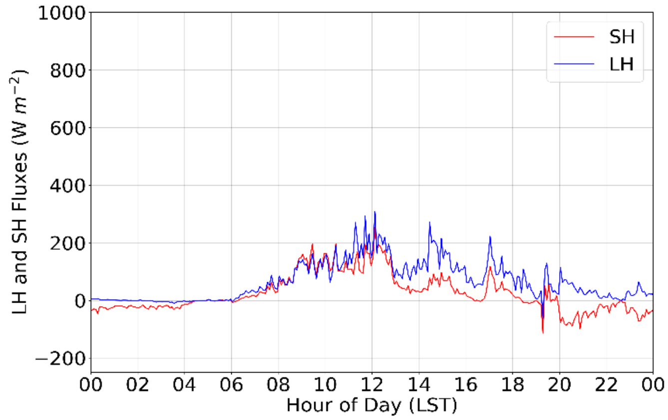

b)

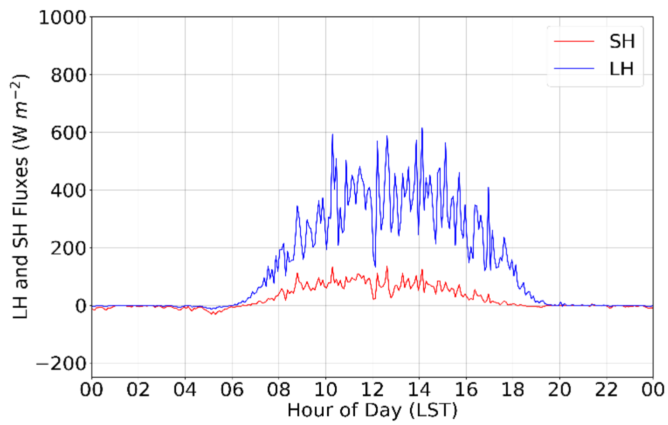

c)

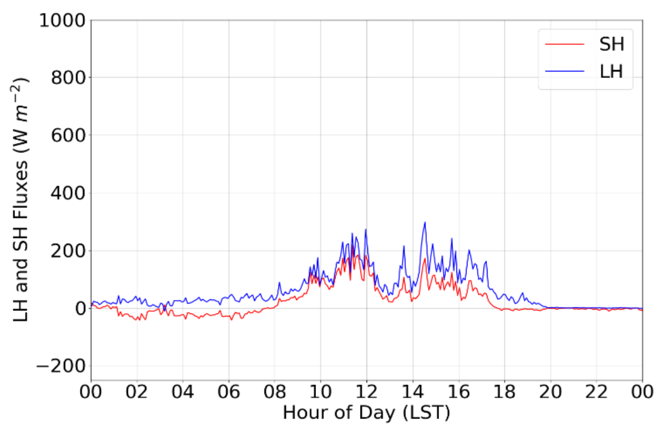

Accepted for publication in *Bulletin of the American Meteorological Society.* DOI 10.1175/BAMS-D-20-0041.1.

d)

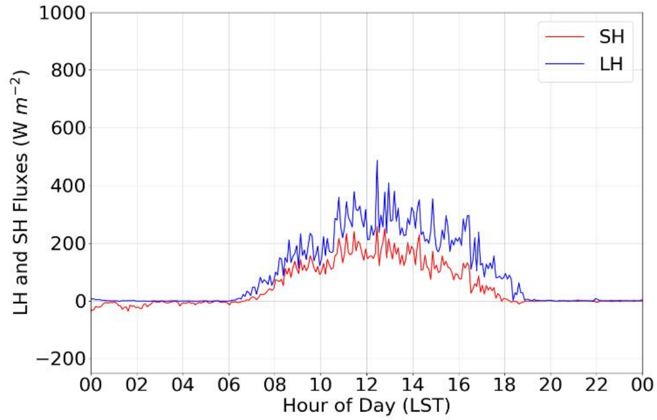

e)

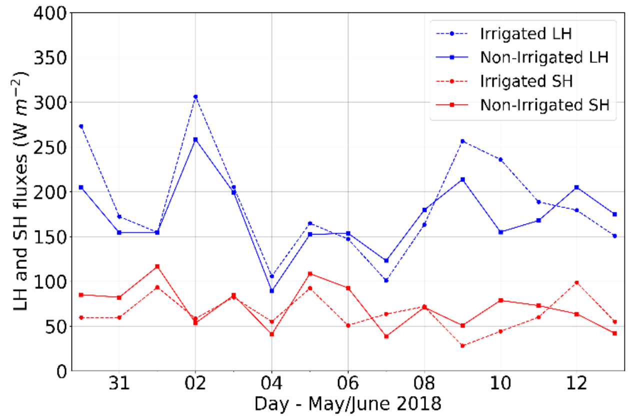

f)

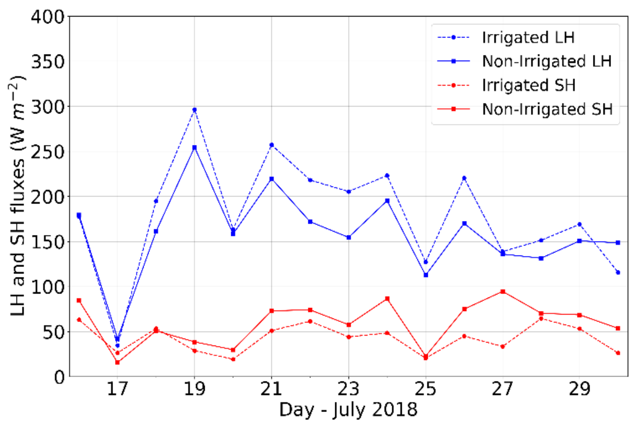

Fig. 4a-f. ISFS irrigated site 1 diurnal variation of surface fluxes for a select date during: a) IOP1 (06 June) and b) IOP2 (24 July); c, (07 June) d) (24 July) same as a, b but for non-irrigated ISFS site 8. Daily-averaged latent and sensible heat fluxes are for all irrigated and non-irrigated sites: e) IOP1 and f) IOP2. To capture fluxes during sunrise to sunset and to synchronize with radiosonde launches, daily averages were calculated for a period from 0500 LST to 1900 LST.

Accepted for publication in *Bulletin of the American Meteorological Society.* DOI 10.1175/BAMS-D-20-0041.1.

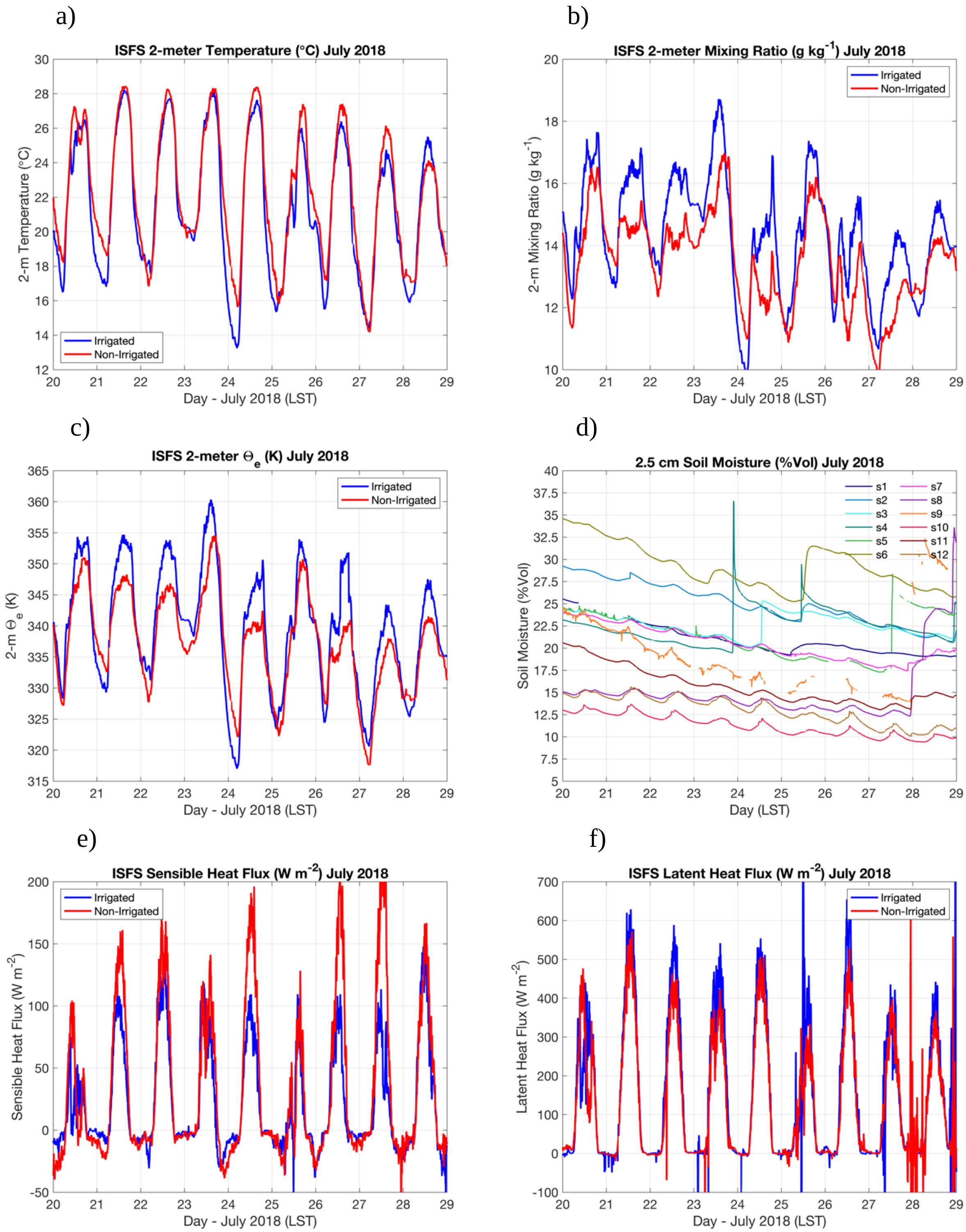

Fig. 5a-f. Average (except for d): a) temperature, b) mixing ratio, c) equivalent potential temperature, d) soil moisture for each ISFS site, e) sensible heat flux, and f) latent heat flux over irrigated and non-irrigated ISFS sites during IOP2. In the panel 5d, irrigated sites 1-6 are shown as s1-s6 with blue-ish colors which show higher soil moisture while non-irrigated sites 7-12 are shown as s7-s12 with red-ish colors with lower soil moisture.

Accepted for publication in *Bulletin of the American Meteorological Society*. DOI 10.1175/BAMS-D-20-0041.1.

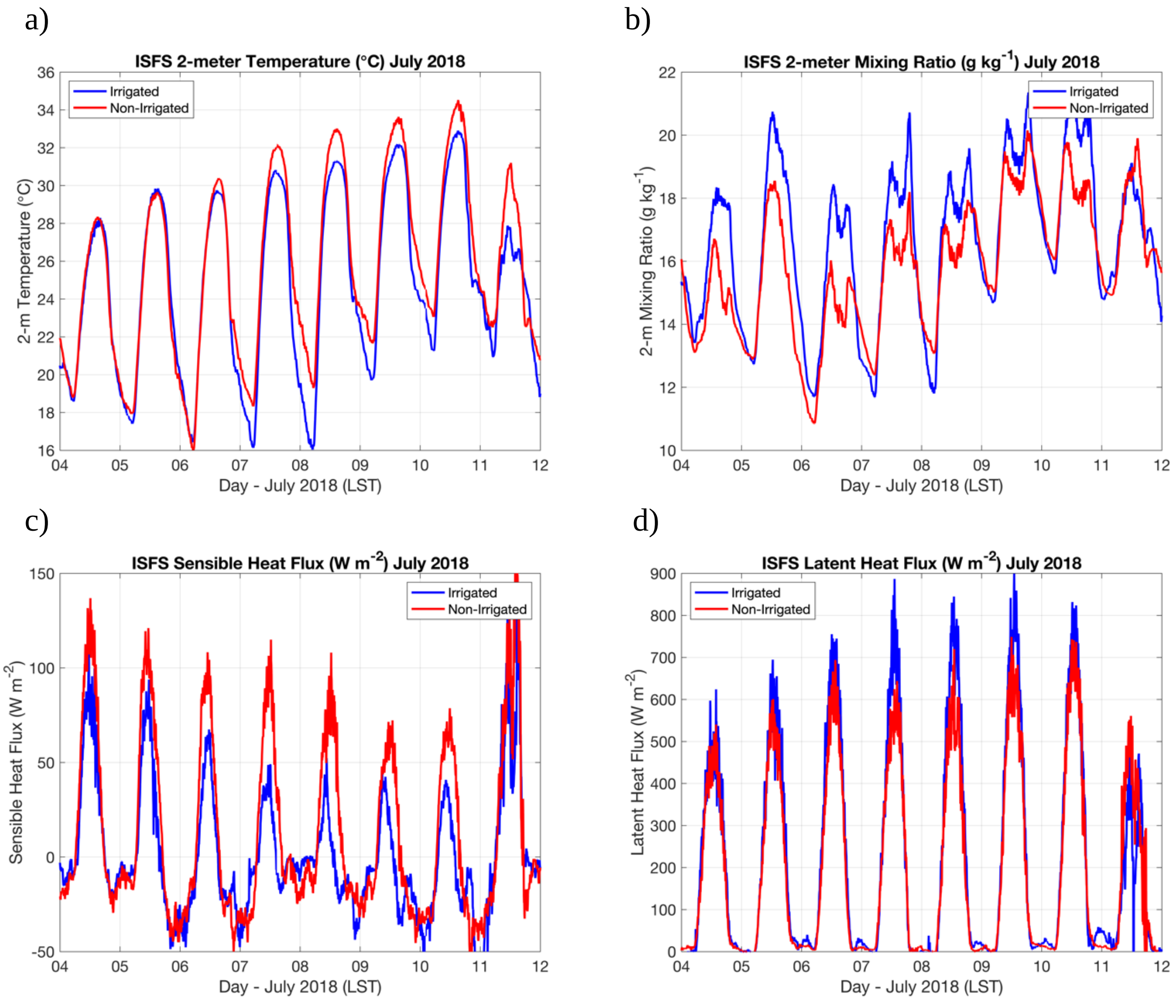

Fig. 6a-d. Average: a) 2-m temperature; b) 2-m mixing ratio; c) sensible heat flux, and d) latent heat flux for irrigated and non-irrigated ISFS sites during the *inter-IOP* period.

Accepted for publication in *Bulletin of the American Meteorological Society*. DOI 10.1175/BAMS-D-20-0041.1.

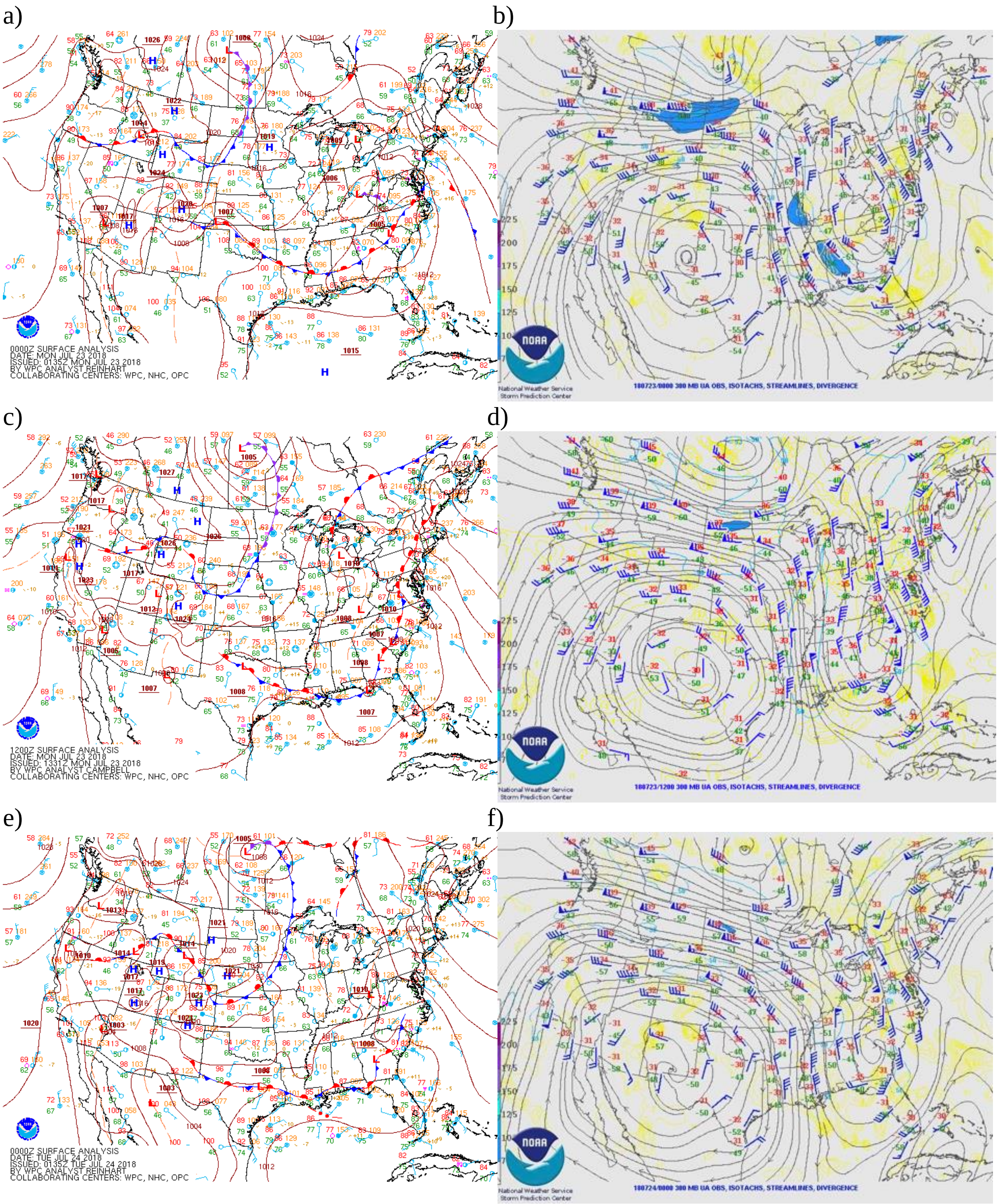

Fig. 7a-f. Synoptic-scale conditions over the conterminous USA provided by NOAA's Weather Prediction Center and Storm Prediction Center. Surface analysis (left column) and 300 hPa analysis (right column) at: a, b) 1800 LST 22 July (0000 UTC 23 July) 2018; c, d) 0600 LST (1200 UTC) 23 July 2018, and e, f) 1800 LST 23 July (0000 UTC 24 July) 2018. Blue shaded areas and yellow lines are showing jet streaks and divergence, respectively.

Accepted for publication in *Bulletin of the American Meteorological Society.* DOI 10.1175/BAMS-D-20-0041.1.

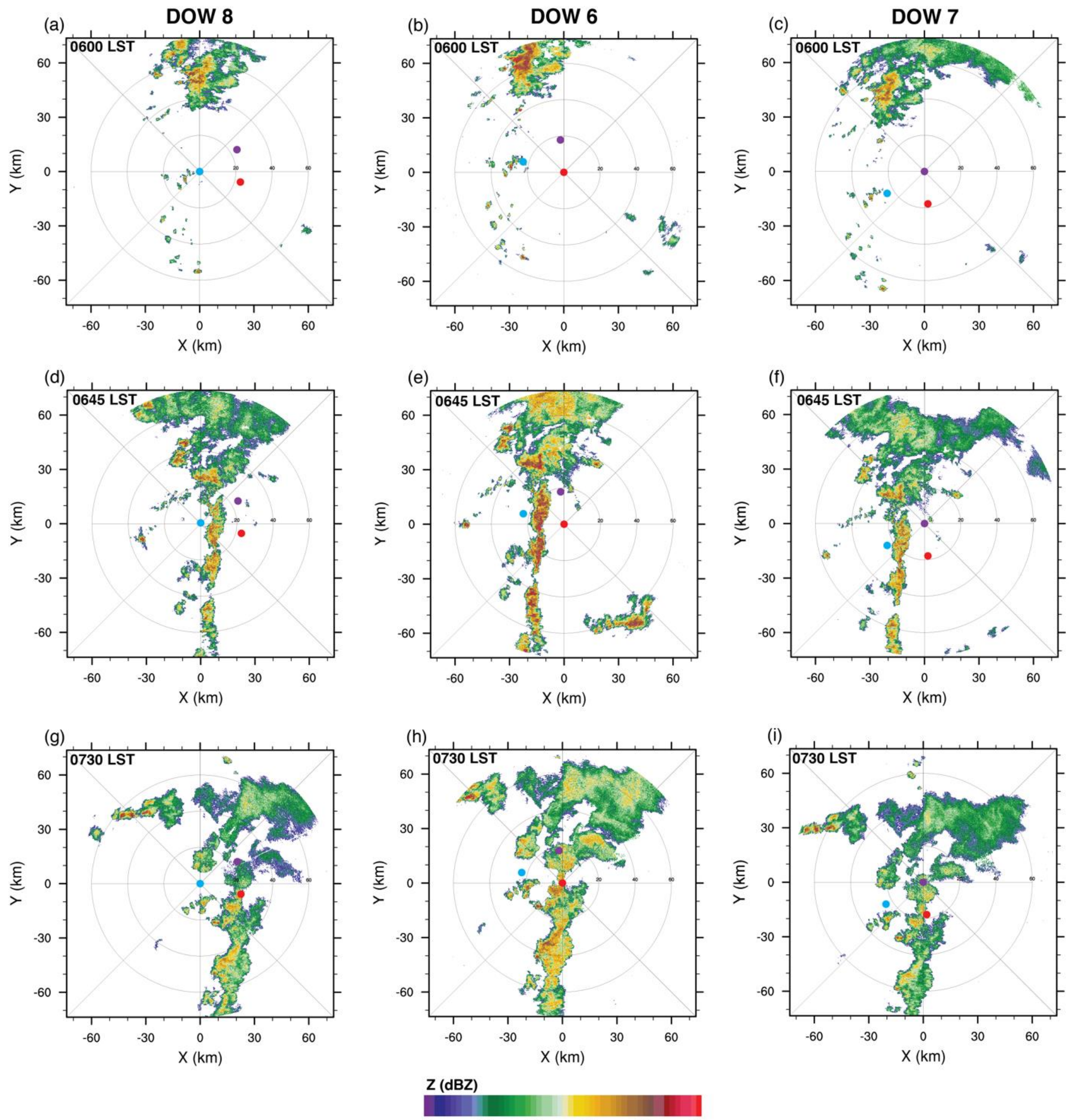

Fig. 8a-i: Radar reflectivity (Z) at 1.2° elevation from DOW8 (left column), DOW6 (center column), and DOW7 (right column) radar for a,b,c) 0600 LST; d,e,f) 0645 LST; and g,h,i) 0730 LST on 23 July 2018. The locations of the radars are shown with a blue dot (DOW8), red dot (DOW6), and purple dot (DOW7). North is located towards the top. For clarity, radar reflectivity below 2 dBZ is not plotted.

Accepted for publication in *Bulletin of the American Meteorological Society*. DOI 10.1175/BAMS-D-20-0041.1.

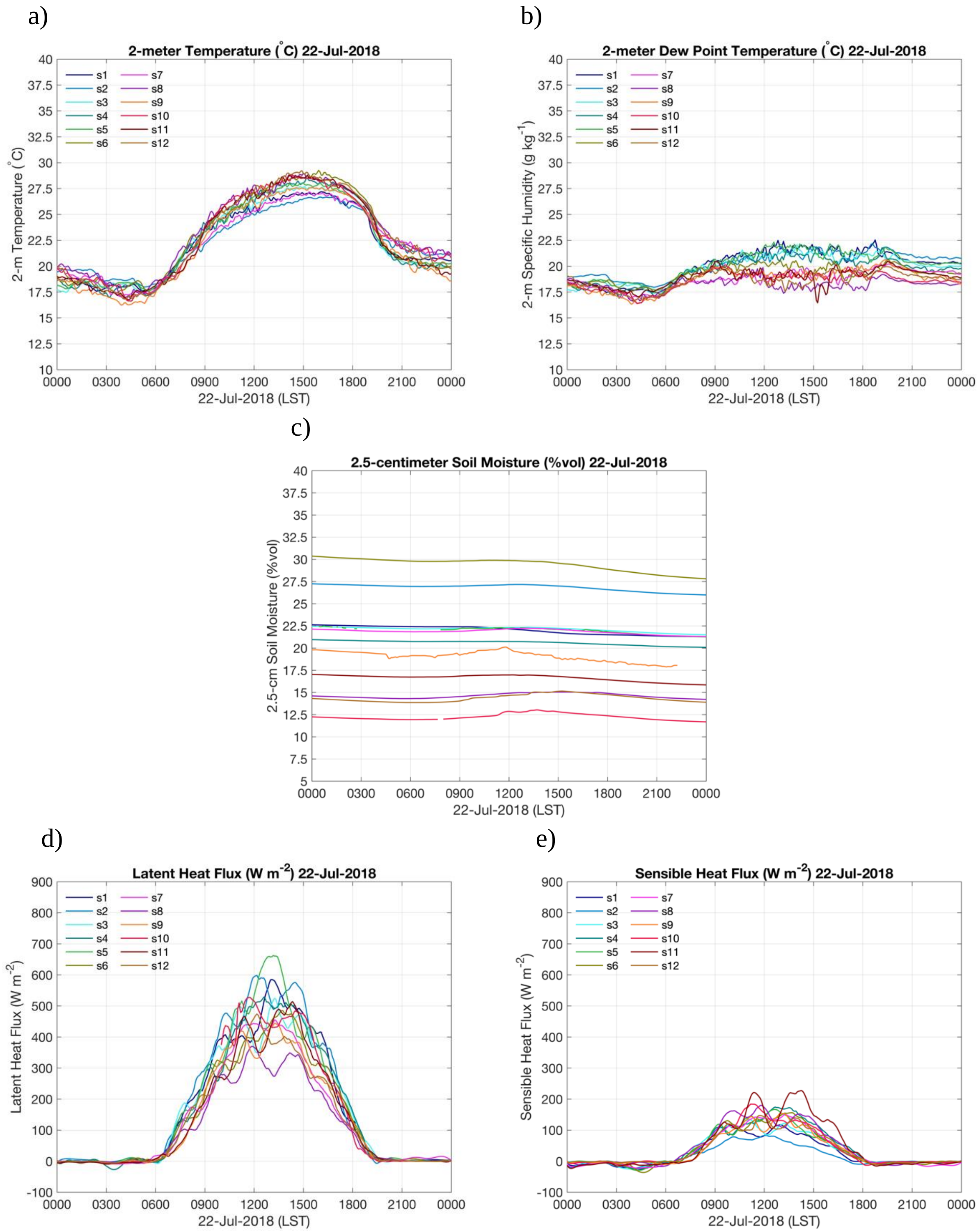

Fig. 9a-e. ISFS site data on 22 July 2018 for: a) 2-m temperature, b) 2-m mixing ratio, c) soil moisture, d) latent heat flux, and e) sensible heat flux over irrigated [sites 1-6 (shown as s1-s6 with blue-ish colors)] and non-irrigated [sites 7-12 (shown as s7-s12 with red-ish colors)] ISFS sites.

Accepted for publication in *Bulletin of the American Meteorological Society*. DOI 10.1175/BAMS-D-20-0041.1.

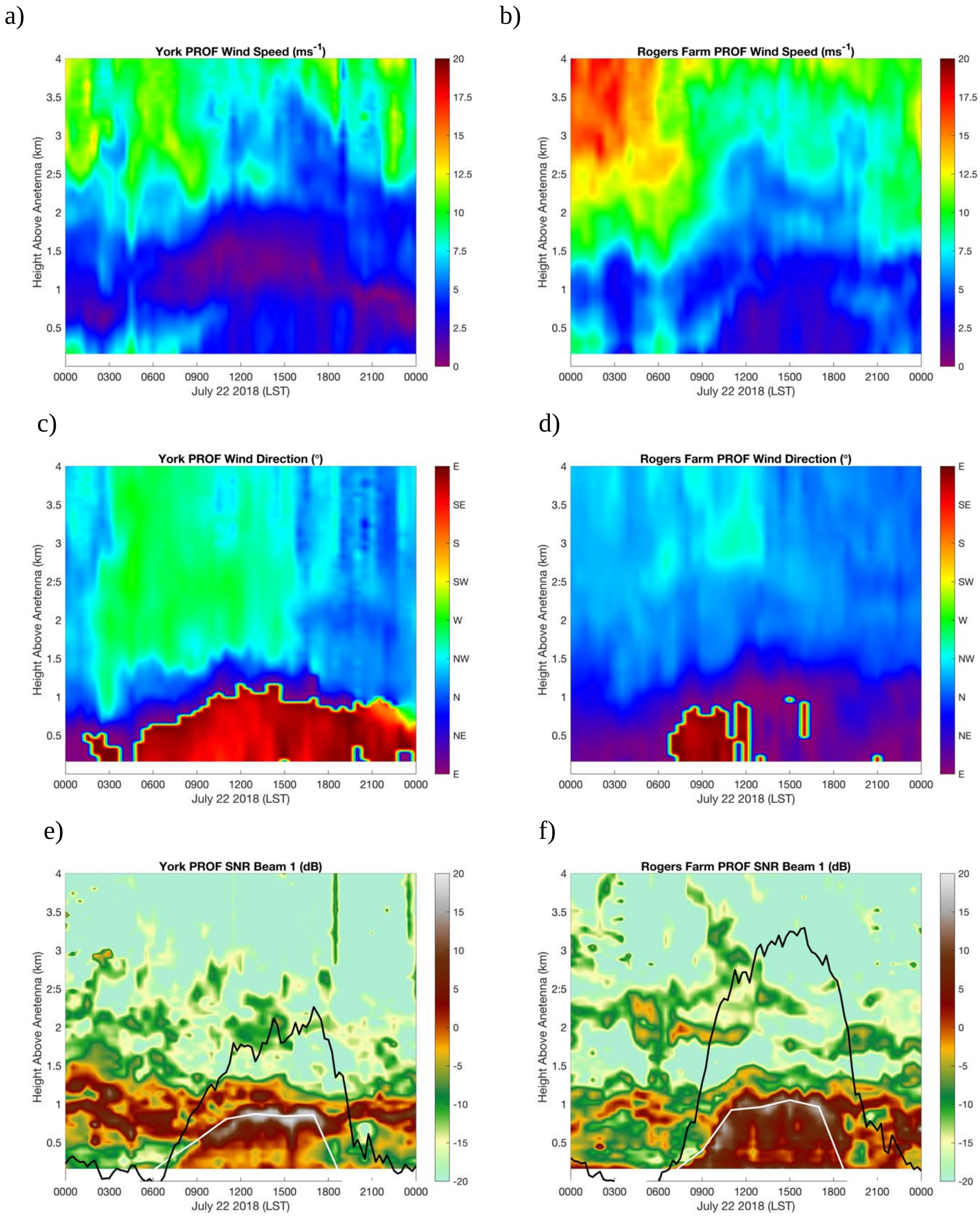

Accepted for publication in *Bulletin of the American Meteorological Society*. DOI 10.1175/BAMS-D-20-0041.1.

g) h)

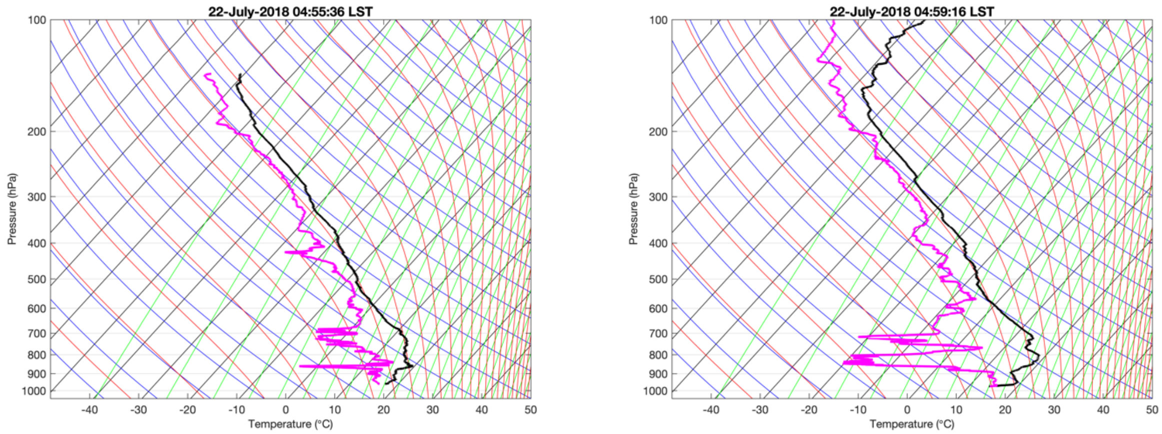

Fig. 10a-h. 915 MHz wind profiler plots for York (left column) and Rogers Farm (right column) ISS sites for 22 July 2018: a, b) wind speed; c, d) wind direction; e, f) signal-to-noise ratio (SNR) with boundary layer height calculated from sounding using critical Richardson number (white line) and lifting condensation level (LCL) (black line) and g, h) skew-T and log*p* from radiosondes from the first sounding of the morning (~1100 UTC, ~0500 LST).

Accepted for publication in *Bulletin of the American Meteorological Society*. DOI 10.1175/BAMS-D-20-0041.1.

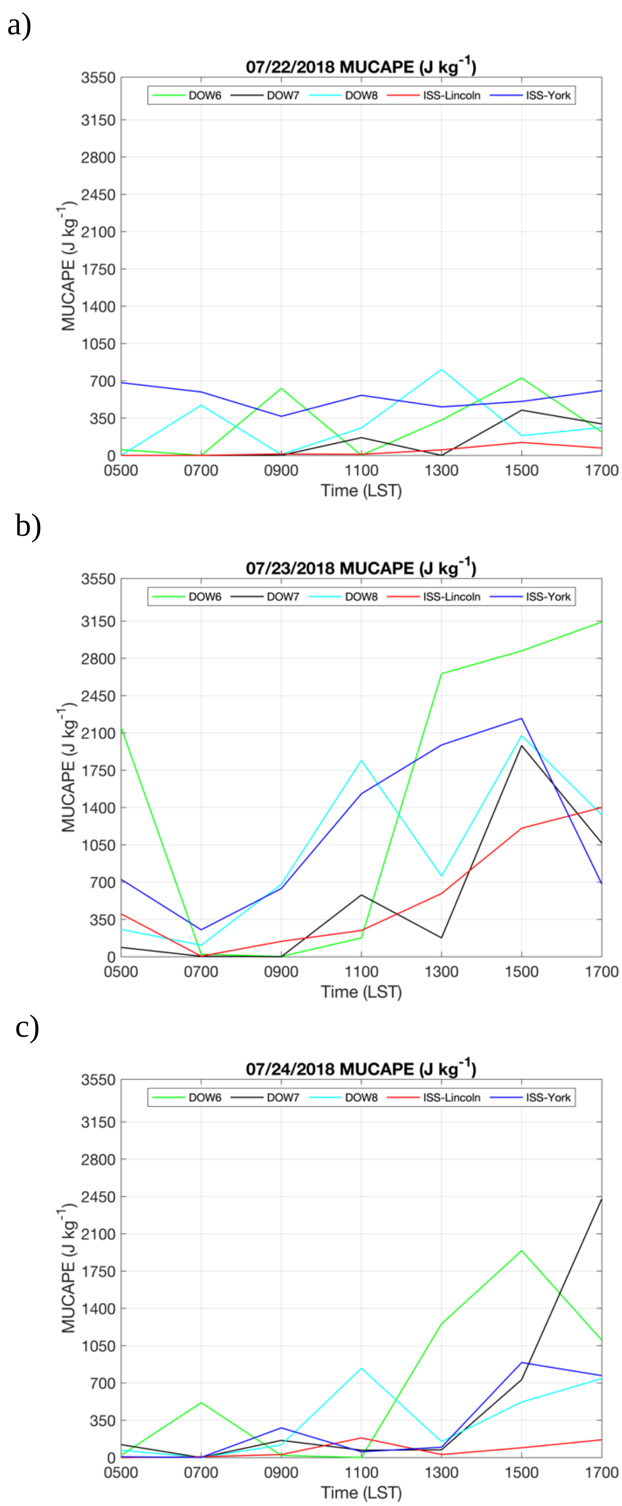

Fig. 11a-c. MUCAPE calculated from daily soundings at the two ISS and three DOW sites for: a) 22 July 2018, b) 23 July 2018, and c) 24 July 2018.

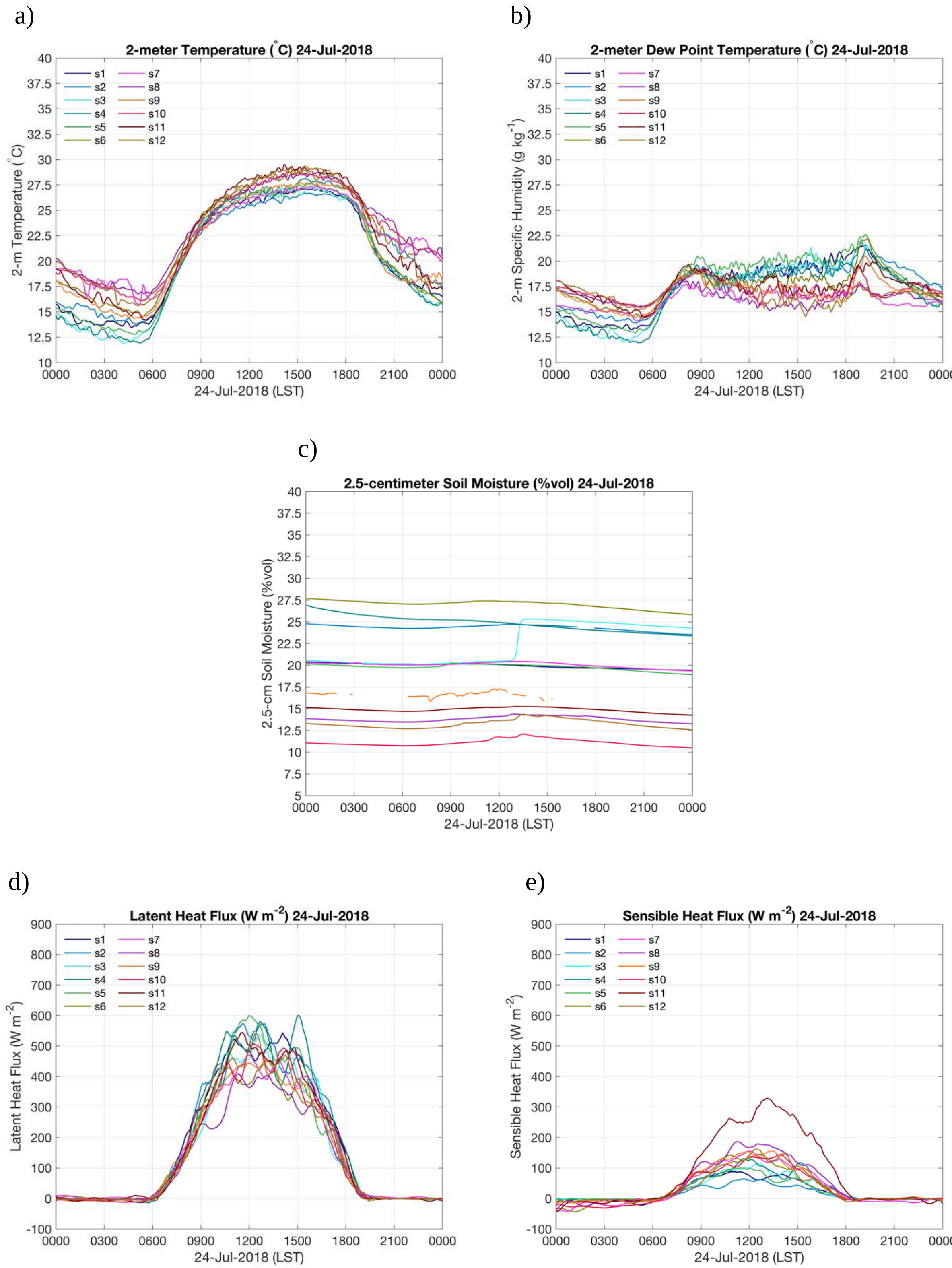

Fig. 12a-e. Same as Fig 9a-e but for 24 July 2018.

Accepted for publication in *Bulletin of the American Meteorological Society*. DOI 10.1175/BAMS-D-20-0041.1.

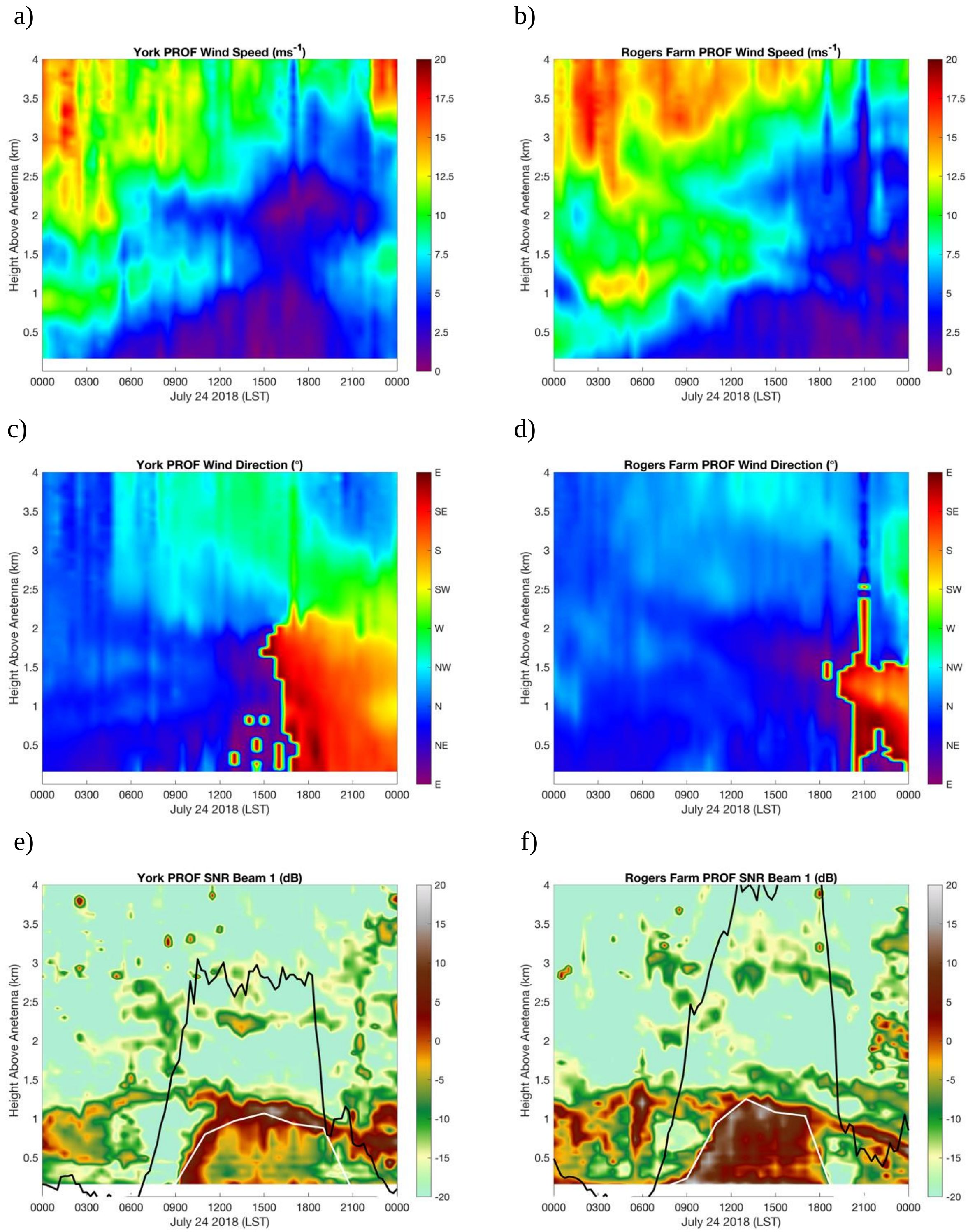

Fig. 13a-f. Same as Fig. 9a-f but for 24 July 2018.

Accepted for publication in *Bulletin of the American Meteorological Society.* DOI 10.1175/BAMS-D-20-0041.1.

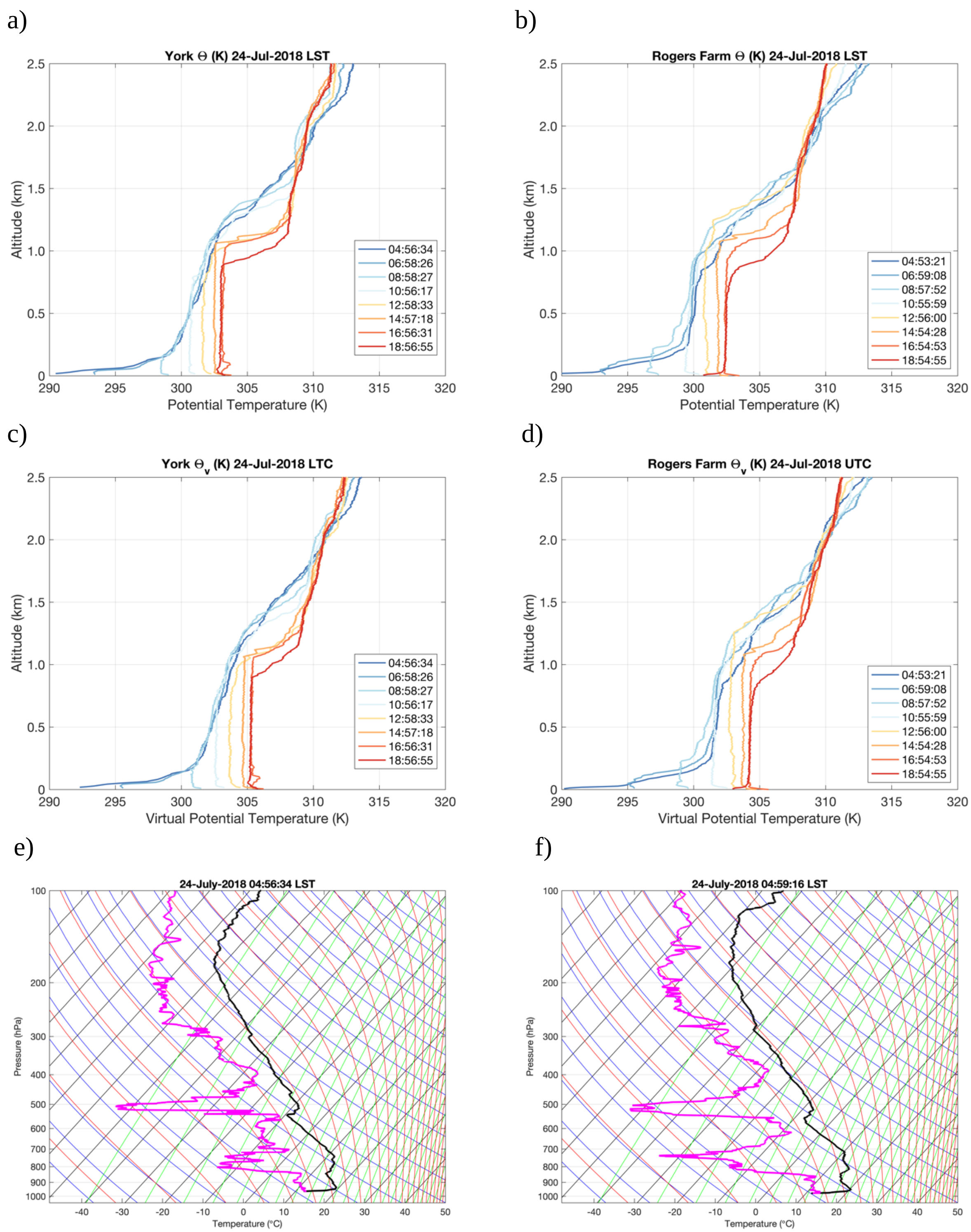

Fig. 14a-f. Radiosonde profiles on 24 July 2018 from the York (left column) and Rogers Farm (right column) ISS sites 8 times daily from ~0500 LST to ~1900 LST : a, b) Boundary layer and lower free atmosphere θ; c, d) boundary layer and lower free atmosphere θ_v; and e, f) air temperature and dew point temperature through the troposphere.

Accepted for publication in *Bulletin of the American Meteorological Society*. DOI 10.1175/BAMS-D-20-0041.1.

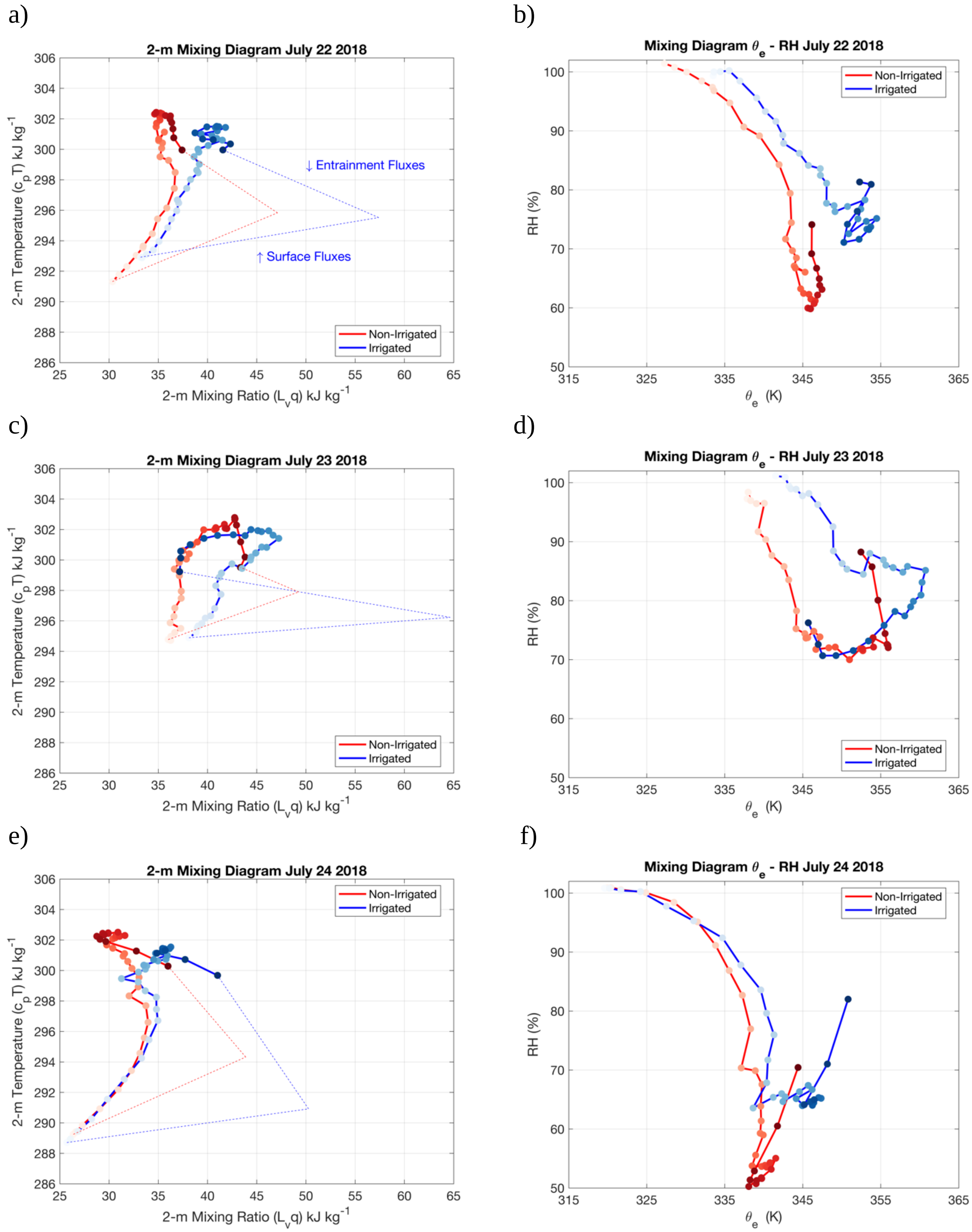

Fig. 15a-f. Mixing diagrams, or the temporal evolution of the moisture and heat terms of the surface moist static energy (left column) and relative humidity-θ_e space (right column) for: a, b) 22 July 2018; c, d) 23 July 2018, and e, f) 24 July 2018. The temporal evolution is from sunrise to sunset with each segment lasting 20 minutes and the dots getting darker as the day gets longer.

Dotted lines in a, c, and e show the Bowen Ratio slope of the surface (lower) and entrainment (upper) for irrigated (blue) and non-irrigated (red) cropland.

Accepted for publication in *Bulletin of the American Meteorological Society*. DOI 10.1175/BAMS-D-20-0041.1.

a) b)

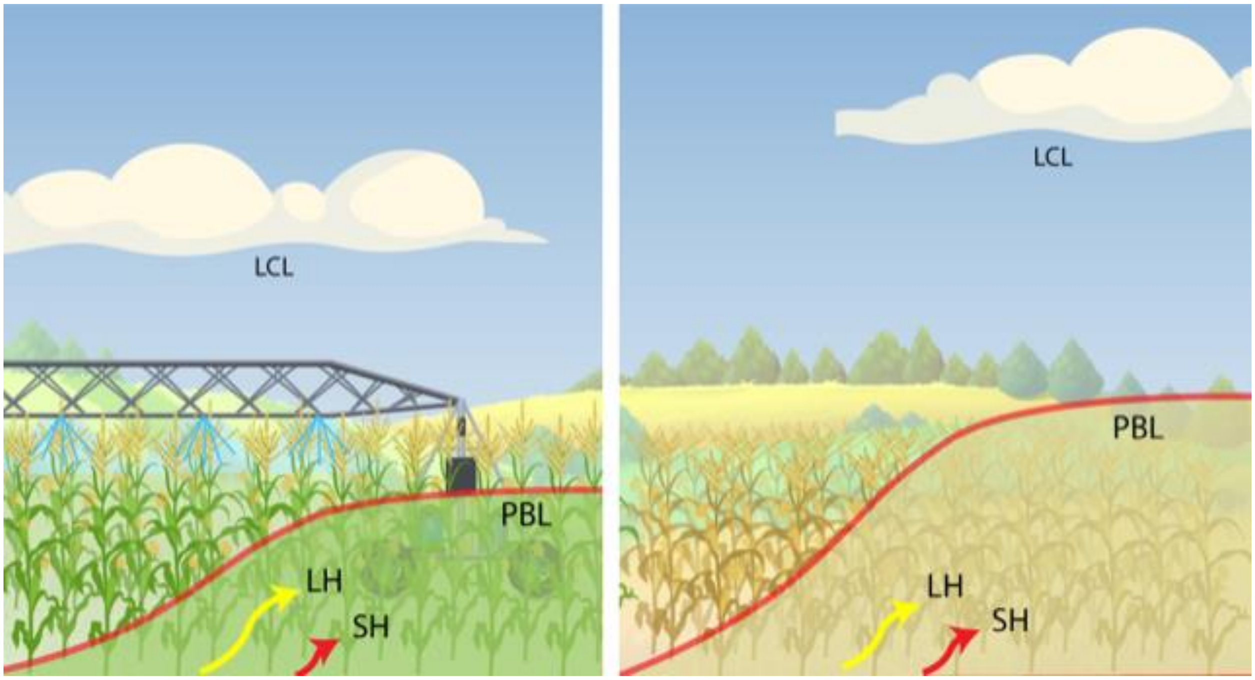

Figure 16a-b. A conceptual diagram of changes in Lifting Condensation Level (LCL), Planetary Boundary Layer (PBL), Latent Heat Flux (LH), and Sensible Heat Flux (SH) over: a) irrigated and b) non-irrigated land use land cover. In the Figure 16a, due to irrigation, latent heat flux is higher and sensible heat flux is lower. On the other hand, over non-irrigated land use (Figure 16b) LH is higher compared to SH but the difference between the two (LH vs. SH) is much smaller. Overall, SH is greater over non-irrigated land use compared to irrigated land use. This condition also impacts depth of the PBL and resulted in higher PBL height over non-irrigated land use. Relatively higher LH and moistness over irrigated land use resulted in lower LCL compared to non-irrigated land use.

Accepted for publication in *Bulletin of the American Meteorological Society.* DOI 10.1175/BAMS-D-20-0041.1.